DROP INTERFACE SHAPE RECONSTRUCTION USING STEREOSCOPIC

SPECKLE MEASUREMENTS

A Thesis

by

HUGO GIORDANO

Submitted to the Office of Graduate and Professional Studies of
Texas A&M University
in partial fulfillment of the requirements for the degree of

MASTER OF SCIENCE

Chair of Committee,	Edward White
Committee Members,	Mohammad Naraghi
	Raffaella Righetti
Head of Department,	Srinivas Vadali

May 2021

Major Subject: Aerospace Engineering

ABSTRACT

A stereoscopic speckle imaging technique is developed for measuring three-dimensional instantaneous profiles of asymmetric liquid drops on rough surfaces. The surface roughness creates a speckle pattern that allows for the cross-correlation of images with and without the drop present. The difference in the images captured using two stereoscopic cameras are encoded as shift vectors caused by light refraction across the drop interface. The drop profile is reconstructed using a simplex optimization procedure to find the shape for which the calculated shift vectors best match the measured shift vectors. An error analysis was performed and found contact angle error to be within -3.4° and 2° for one standard deviation. The stereoscopic approach is shown to better reconstruct contact angles as compared to the single camera method while simultaneously increasing the maximum measurable drop contact angle from 50° to 70°. This is due to the angled stereoscopic cameras delaying the internal reflection of light refracting through the water-air interface. Drop volume, height, and pinning force estimates generated using the approach are analyzed and discussed.

DEDICATION

To my mother and my father, and to Zamira for all your love and support

ACKNOWLEDGMENTS

I extend humble thanks to the many people who helped me along this journey. Firstly and formostley, I want to thank my advisor Dr. Edward White for all his guidance, wisdom, patience, and much more. Your mentorship has gone far beyond the laboratory and I hope to someday be as good of a mentor and a leader as you were to me.

I would also like to thank the other members of my committee, Drs. Mohammad Naraghi and Raffaella Righetti for their input in my research, along with many provocative questions that encouraged further exploration.

Finally, Roger Simon and Eleazar Herrera Hernandez were invaluable in the assistance the provided in the completion of this thesis.

CONTRIBUTORS

Contributors

This work was supervised by a thesis dissertation committee consisting of the chair Professor Edward White and Mohammad Naraghi of the Department of Aerospace Engineering and Professor Raffaella Righetti of the Department of Electrical Engineering.

All other work conducted for the thesis was completed by the student independently.

Funding Sources

TABLE OF CONTENTS

LIST OF FIGURES

LIST OF TABLES

TABLE   Page

1. INTRODUCTION AND LITERATURE REVIEW

1.1 Drop Physics

When a sessile liquid drop rests on a level surface, surface tension and contact angle hysteresis creates a pinning force that prevents the drop from sliding along the surface. When acted upon by wind forcing or gravity, the drop shape changes to increase the pinning force and resist the external forcing. Faced with increased velocities or steep inclines, the pinning forces are eventually overcome and the drop depins and runs along the surface. This phenomenon has been the subject of countless studies starting with Laplace's (1805) theory of capillarity and continuing through today.

Having the ability to predict when drops depin and run back along surfaces is useful in many practical applications such as aircraft icing prediction, heat exchangers, fuel cells, and other industrial processes. In aircraft icing, rime ice is formed when a liquid-phase drop hits the surface of a wing and immediately freezes. In less extreme conditions, drops run back a certain distance before freezing. This is called glaze icing and is much harder to model than rime icing (Kraj and Bibeau, 2010). In industrial heat exchangers, thermal efficiency can be improved by increasing the drop runback distance (Strizhak et al., 2017). While predicting depinning can significantly improve the efficiency and safety of industrial machines across a wide array of disciplines, determining characteristic runback distances remains unreliable.

The contact angles between a drop and a surface are the key to drop stability. Drop depinning is governed by the balance of forcing terms and pinning forces acting on a drop. The surface pinning force a water droplet exerts on a surface is a function of the

1

surface tension and contact angle and is given by the integral

$$\vec{F} = \gamma \oint \cos \theta(s) \, \hat{n}(s) \, ds \tag{1.1}$$

where γ is the surface tension, $\theta(s)$ is the contact angle between the drop and the surface, $\hat{n}(s)$ is the unit normal vector to the contact line in the surface plane, and ds is the differential length element along the perimeter of the contact line. Equation 1.1 is correct for three dimensions and yields $\vec{F}$ with units of force. The two dimensional (2D) equivalent gives force per unit depth and is instructive to consider. Figure 1.1 shows the advancing contact angle θ_a is the maximum contact angle on the advancing side of the drop and the receding contact angle θ_r is the minimum contact angle on the receding side. Contact angle hysteresis is defined as the difference between the two angles $\theta_a - \theta_r$. The difference between the cosines of the two angles $\Delta \cos \theta = \cos \theta_r - \cos \theta_a$ is more useful measure as the maximum pinning force per unit depth is $\vec{F}_{max} = \gamma \Delta \cos \theta$ (Macdougall and Ockrent, 1942). Contact angle hysteresis is primarily caused by surface roughness, but chemical heterogeneities, surface deformation, liquid adsorption and retention, molecular rearrangement on wetting, and interdiffusion can be other factors (Eral et al., 2013).
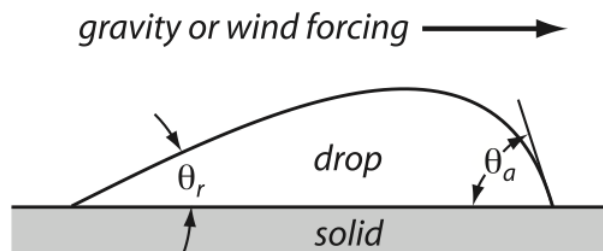
Figure 1.1: 2D drop profile with advancing and receding contact angles. Reprinted with permission from (Schmucker and White 2007)

While the basic explanation of how surface tension pins drops to surfaces are well known, the complexity of the phenomenon makes predictions of depinning conditions very difficult. A key reason is that the three-dimensional (3D) shape of the drop is necessary for modeling the pinning force but measurement of 3D drop interface shapes are very limited. Most measurements reported in the literature are side-view images that can only estimate the pinning force from the contact angle hysteresis.

This research aims to improve depinning predictions by providing a full 3D model of the drop. Previous attempts to predict runback rely almost entirely on the contact angle hysteresis and break down when faced with large advancing contact angles and surface slopes. A full drop profile forgoes the 2D assumptions and provides the contact angle at every point along the drop, instead of just two.

1.1.1 Drop Depinning Studies

Macdougall and Ockrent (1942) first identified the importance of contact angle hysteresis in determining the critical inclination angle for gravity-forced drop depinning. They viewed drops from the side and measured contact angles at the highest and lowest positions on the contact line. They claimed that these angles, θ_r and θ_a respectively, are always the smallest and largest contact angles formed by the drop. Dussan and coworkers (1983, 1985, 1987) sought to explain these results in a 3D analytical theory and paved the way for future drop stability studies. Dussan V. and Chow (1983) developed a full model for drop pinning forces using lubrication theory and concluded that contact angle hysteresis was the single most important factor in determining drop forces. Dussan V. and Chow (1983) and Dussan V. (1985) expanded their solution's capability by eliminating the lubrication theory constraint of small surface slopes, but still required small advancing contact angles and small hysteresis (less than 10°). Dussan (1987) studied the effects of wind shear on drop stability, concluding that drop viscosity has no effect on critical

3

depinning configuration. Simulations by Dimitrakopoulos and Higdon (1997) set out to validate Dussan's theories without such restrictive constraints. They concluded that the model proposed by Dussan had a very narrow useful range, only finding agreement in the limits $\Delta\theta \ll \theta_a \ll 1$. This was speculated to be a result of Dussan's asymptotic expansions, which break down under realistic conditions.

A variety of recent studies on the phenomenon are by Quéré et al. (1998), ElSherbini and Jacobi (2006), Berejnov and Thorne (2007), and Chou et al. (2012). Quere et al. developed and tested a depinning model for drops with small contact angle hysteresis in the low-Bond-number limit over a wide range of advancing and receding contact angles. Their work was limited to volumes less than 30 μL and diverges with larger drop sizes. ElSherbini and Jacobi provided an analytical model to predict critical runback angles based on modified equations from Dussan (1987), but follow similar assumptions and require small contact angle hysteresis and symetric drop shapes. Berejnov and Thorne show experimental results on evolution of contact line shape and contact angle hysteresis as inclination angle changes. Chou et al. performed similar experiments to Berejnov and Thorne and ran numerical simulations to validate them.

Amirfazli and coworkers authored several papers detailing experimental observations of drop depinning. In one of these, Pierce et al. (2008) notes that two-dimensional contact angle hysteresis is not sufficient for predicting drop stability. Further, they claim that θ_a and θ_r are not the largest and smallest angles observed on a drop for all conditions as previously thought. They note previous tilted plate experiments such as those by Macdougall and Ockrent (1942) or Bikerman (1950) are not sufficient for predicting drop runback, especially in high-hysteresis systems. This two-dimensional simplification only roughly sketches the drop shape and in doing so only roughly predicts the pinning forces (Milne and Amirfazli, 2009). The two-dimensional assumptions are that the drop

is symmetric about the forcing direction and the integral for the forces is only sampled at two locations, the advancing and receding contacts. A three-dimensional measurement of the drop shape would not require any assumptions about the drop symmetry and would provide a more accurate pinning force estimate.

1.2   Drop Shape Measurement Techniques

The methods used in drop depinning experiments have remained largely unchanged for decades. The most common experimental setups involve observing drop parameters from the top and side to produce depinning correlations. Almost seventy years ago Bikerman (1950) used a top-view camera to make correlations between the tilt angle of the surface, volume of the drop, and drop shapes. He furthered the conclusions by Macdougall and Ockrent (1942) through photographs and visual observations that an increase in contact angle hysteresis increases a drop's ability to resist motion along a surface. A top-view and side-view camera observing a tilted plate became a staple for studying drop behavior as the top-camera captures the changes in the drop spreading while the second camera captures the contact angle hysteresis. The tilted plate is used to deform the drops as the exact gravitational forcing term applied is easily calculated using the tilt angle.

Extrand and Kumagai (1995) used this setup with digital cameras and gathered data on contact angles and drop shapes on titlable plates. Podgorski et al. (2001) used only a top-view camera to qualitatively study the dynamics of the contact line as a drop begins to run back. The experiments by Milne and Amirfazli (2009) also used a single side-view camera to measure the contact angles and draw correlations between the hysteresis and runback thresholds. Lacking more complete 3D data, these authors used an empirical factor in his analysis.

Rio et al. (2005) used a laser line-scanning technique to measure the profiles of drops sliding down an inclined glass plate. The technique allows for full reconstruction of

moving drops, but has limited use cases. The drops must be in motion, the drops are assumed to have a constant drop shape and velocity as they slide, and the surface must be transparent and smooth. This does not allow for stability measurements of static drops or on rough aluminum surfaces or with variable contact lines.

To address the need for a robust 3D measurement procedure for drops, Schmucker and White (2007) created a technique to calculate the full drop profile under wind or gravity forcing. The method provided the first instantaneous measurements of full 3D drop interface profiles on non-transparent surfaces and works on stationary and moving drops of various shapes. Schmucker and White (2007) took sets of surface speckle images, starting with a speckled image of a dry aluminum surface as a grayscale control image. Then drops were placed on the surface and additional grayscale images are acquired. A speckle pattern in this context refers to the constructive and destructive interference caused by a rough surface reflecting a coherent beam of light with spatially random but not temporally varying phase. This leads to a steady pattern of light and dark speckles in the image plane. The randomness of the pattern assures sample areas of an image are unique with respect to the whole image and that the pattern can be identified after refraction across an interface as it is solely dependant on the local surface roughness. Schmucker and White (2007) used images of surface speckle with and without a drop present, matching the speckle patterns between the two images using mage correlation techniques.

Reconstructing drop interface shapes from the speckle images proceeds through several steps. First, the contact line of the drop is identified. Each drop image is subtracted by the control image and this makes every pixel outside the drop have a difference value of zero. All of the interior pixels have non-zero differences and this makes contact line identification straightforward. Second, once the contact line is identified, the interior space of the drop is mapped onto the unit disk. To do this, an elliptical grid is generated that maps

each (x, z) point in physical space to an (r, θ) point on the unit disk. The elliptical grid is used so that grid lines intersect the contact line at 90° to simplify later calculation of the contact angle. An elliptic grid used by Schmucker and White (2007) would typically include 20 radial lines and 40 circumferential lines.

Speckle shift vectors are measured at each of the intersections of radial and circumferential lines. The shift vector field was measured using cross correlation between the control and drop images. A square subregion of the drop image is taken about each grid location and a correlation coefficient is calculated by convolving the selected subregion with the control image. The difference between the grid location and the location on the control image that yields the largest correlation coefficient is taken as the most likely shift vector. For highly skewed subregions the calculated shift vectors may be incorrect, which were removed via outlier detection. Outliers were found by the numerical value of the correlation coefficient being too low or if the vector magnitudes and directions did not match the trends from the surrounding grid locations.

Schmucker and White (2007) developed a relationship between the drop profile and speckle shift vector measured by the camera lens. By tracing a ray of light reflecting off of the surface, the difference in position as viewed by the camera lens between the speckle pattern in the control image to the drop image is calculated. They then show that the measured pixel shift vector, $\overrightarrow{s}(x, z)$, can be related to the drop height (y) and surface slope $(|\nabla y|)$ at each (x, z) pixel location as:

$$\overrightarrow{s}(x, z) = -y \tan[\tan^{-1}(|\nabla y|) - \sin^{-1}(\frac{n_{air}}{n_{water}}) \tan^{-1}(|\nabla y|)]\frac{\nabla y}{|\nabla y|} \qquad (1.2)$$

Using the shift vectors and the relation between shift vectors to local drop height and slope found in Equation 1.2, an optimization procedure was run to best fit the drop parameters to the measured shifts. The solution was constructed of a linear combination

of Fourier-Bessel series and a spherical cap model. Schmucker et al. (2012) tested this technique over a range of drops 50 to 300 μL and tilted plate angles 0° to 30°. For contact angles between 35° and 45° the error between the reconstructed angle and the measured angle stayed within +2° and -7° for $1 - \sigma$ of cases. Drops with a contact angle higher than 50° saw a significant rise in contact angle estimation error with any angle over 60° not able to be measured. Contact angles less than 30° also experienced an increase in measurement error but less significantly than higher angles.

A drop under a forcing condition near depinning may form highly asymmetric profile shapes with contact angles exceeding 50° and this prevents the technique as implemented by Schmucker and White (2007) from being as useful as intended for drop depinning experiments in which large contact angles are observed. The reconstructed drop volumes were also measured to be only 70% to 90% of applied drop volume. The error in measurements is primarily caused by the lack of data around the edges of the drops. When imaging a liquid drop internal reflection increases close to the drop edge which can prevent shift vectors from being measured (Garg and Nayar, 2006). If the drop surface normal becomes greater than 55°, total internal reflection occurs and no data can be captured from that point to the edge of the drop. The loss of data near the drop edges creates significant error at larger contact angle hysteresis as the drop asymmetry prevents the data captured in the center of the drop from accurately predicting the edges.

1.2.1   Research Objective

This research aims to overcome the limitation of the single-camera setup developed by Schmucker and White (2007) by using two stereoscopic cameras. These two cameras will simultaneously capture the advancing and receding sides of the drop from two different angles and delay the onset of internal reflection. This will allow for the interface reconstruction method to gather data closer to the drop contact line and improve

8

the reconstruction quality near the contact line. This will overcome the key limitation of Schmucker's method. To implement the stereoscopic measurements, new camera support hardware will be fabricated and a new set of data processing routines will be created. As part of the software modifications, an open-source digital image correlation program NCorr (Blaber et al., 2015) will be used that samples more data points faster and with better accuracy than previously. Stereoscopic drop images will be captured under various forcing conditions and for different contact line shapes. Reconstructed 3D interface shapes based on these images will be generated and compared to applied drop volumes, side-view profile images, and the single-camera setup developed by Schmucker and White (2007).

2. WIND TUNNEL DESIGN AND OPERATION

The steroscopic speckle imaging system developed as part of this thesis will be used in conjunction with a wind tunnel developed by Schmucker (2012) to study drop depinning due to gravity and wind forcing. To provide the needed capabilities for those experiments, the tunnel is capable of rotating the test section up to $\pm 90°$ and provides full optical access on both sides as well as on top, allowing for multiple cameras to view the drop at various angles. These cameras remain static relative to the test section because the speckle shift measurements rely on the camera lens being the exact same distance from the surface in the control image and subsequent test images. The tunnel also allows for different floor pieces so different materials of variable roughness can be tested. The following sections will present the tunnel design by Schmucker (2012) and the modifications made on the tunnel to allow for stereoscopic camera measurements.

The base of the wind tunnel is constructed using aluminum T-slot framing and supports the motor, optics, and test section as shown in Figure 2.1. The aluminium framing forms a triangular base with vibration dampers on all four legs to minimize outside vibrations from the tunnel. Steel brackets and bolts are used to secure the framing at each frame intersection. Rotary bearings hold the tiltable platform that supports the test section and camera mounts. The tilted platform is connected below the bearing level to keep the axis of rotation directly through the test section. This minimizes drop movement during rotation, which could cause premature run back.

The wind tunnel itself is made almost entirely from 0.25-inch-thick machined acrylic panels. The clear walls allow optical access to the entire test section as well as being light, durable, and cost efficient. The tunnel inlet has a cross section 1 inch tall by 8 inches wide and immediately passes through a honeycomb structure with a length-to-diameter
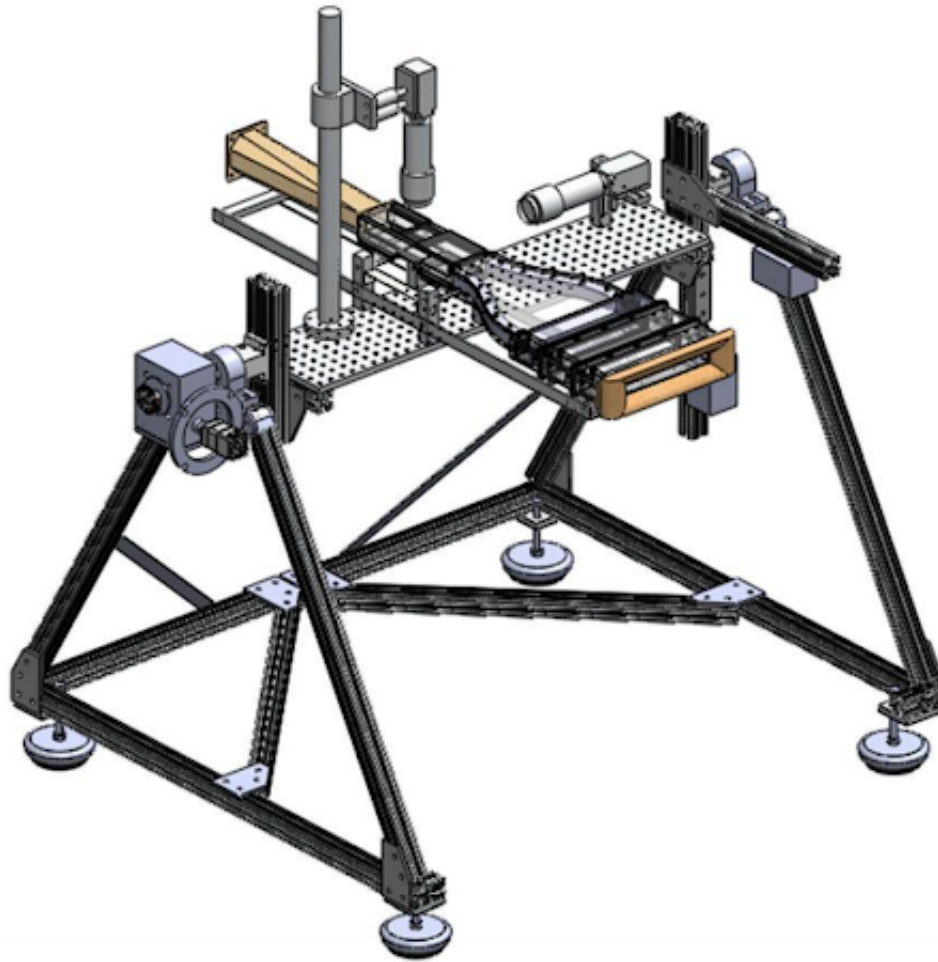
Figure 2.1: Wind tunnel rendering (Schmucker and White 2007)

ratio of four to smooth and properly orient the entering flow. Just after the honeycomb are two metal screens with a 65% open area and a separation of 3.5 inches. The screen openings are smaller than the honeycombs and work to move any turbulent flow to smaller scales which dissipate faster. The tunnel contracts through a 10-inch-long acrylic section reducing the area by a factor of four before reaching the test section with final dimensions 1 inch tall by 2 inches wide. The test section is 10 inches-long. The surface sample is 2 inches long by 1 inch wide and is placed in the center of the test section flush with the

surrounding acrylic floor. This surface sample can be replaced by removing the acrylic floor of the tunnel. The roughness sample used in this work was a sandblasted aluminum block. The sample was measured by a Mituyo SJ-400 roughness tester and has an average roughness of 2.80 μm with a maximum roughness height of 14.3 μm.

Downstream of the test section, the flow is pulled through a small-angle diffuser that prevents any separation from propagating upstream. At the end of the diffuser is an 80 mm Delta axial vaned fan running on a 12 V power supply. The speed of the fan is controlled using a National Instruments USB-6211 data acquisition device and drives the pressure drop that pulls the flow through the tunnel. The flow velocity is measured using two pressure ports just before and after the contraction. The pressure difference between the two straight tunnel sections is measured using an MKS Baratron Type 266A differential capacitive manometer. The measurement error of the system is provided by the manufacturer and is 0.3% of the given pressure readings. Schmucker and White (2012) used a pitot tube to calibrate the tunnel speeds to pressure differences. A proportional gain feedback loop takes the pressure readings from the data acquisition device and maintains a constant velocity in the tunnel.

The tilting plate has $1/4 - 20$ tapped holes on a 1-inch spacing for mounting a top and side view camera in view of the test section as shown in Figure 2.2. The cameras used by both Schmucker and White (2007) and in this experiment were two Pixelink PL-B741U with a resolution of 1280 x 1024 pixels. The cameras are grayscale with an adjustable shutter speed. An 18-108 mm Nikon zoom lens is attached to each camera with a minimum focal length of six inches. To accommodate two steroscopic cameras in this work, a separate camera mount was built using the same T-slot framing as the tunnel base. The cameras are bolted into separate frames that are secured inside one of the aluminum slots. This allows two degrees of freedom: translation along the flow-wise

direction and tilt angle. The cameras be tilted between 5° and 45°, with the lower limit being the result of physical interference between the two camera lenses. The ends of the aluminum T-slot are capped to prevent camera damage in case of slippage. Figure 2.2 shows the stereoscopic camera setup during data capture.
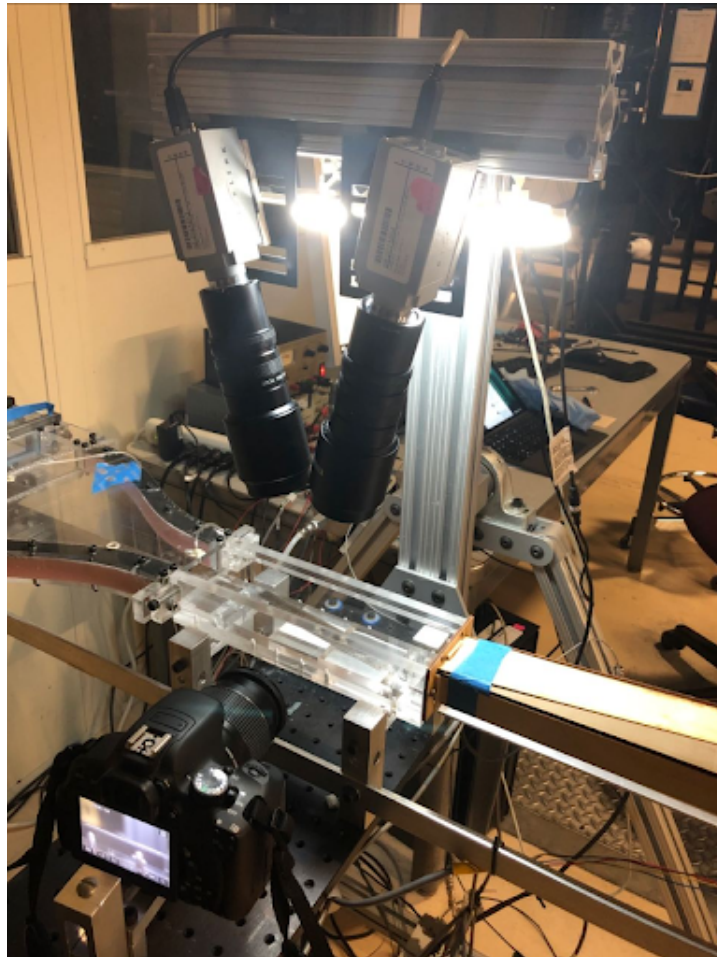
Figure 2.2: Photograph of the wind tunnel with cameras titled at $\pm 13°$

The standard procedure for capturing a drop in the tunnel is as follows. A LabView script takes the live video feed from the two cameras and displays them on the computer

monitor. A drop is placed with a syringe in the center of the cameras' field of view. A second LabView script controls the wind tunnel parameters and takes simultaneous images from both cameras. Each pair of images is saved along with the tunnel parameters such as flow velocity at the time of the photos. After the desired drop shape has been imaged, any remaining liquid is carefully wiped away with a microfiber cloth. A final control image is taken for both cameras to be used in the speckle analysis later. If the cameras were moved or changed magnification to fit the drop, a scale image is taken at the end of the experiment. A ruler is placed in the tunnel and is imaged by both cameras to determine the pixel to inch scale for both the advancing and receding cameras.

3. DROP INTERFACE SHAPE MEASUREMENTS

The drop interface measurements developed in this research are a modification of the method developed by Schmucker and White (2007). Instead of one camera oriented normal to the surface, two steroscopic cameras are placed in line with the flow, one angled from the advancing side and one angled from the receding side. The rough surface is illuminated by a white light source to create a surface speckle pattern and images are taken of the surface with and without the drop present. The method consists of finding the contact line, creating a reconstruction grid, measuring the deformation of the speckle field caused by the refraction though the drop surface, and, finally, reconstructing the drop profile using a simplex optimization method. The method from Schmucker and White (2007) found significant error between the predicted advancing contact angle and measured advancing contact angle above 50° and below 25°. Between 25° and 50° over 60% of the measured contact angles had below 5° error. Outside of the middle range, however, the average error increased dramatically. Receding contact angles below 30° were more likely to be overestimated while advancing contact angles larger than 50° became significantly underestimated. Advancing angles larger than 60° were not able to be captured at all. The main objective of this work is to develop an improved drop reconstruction method that can more accurately measure drop contact angles above 50° while maintaining equal or better measurement accuracy for contact angles less than 50°. The following sections will describe the steps of the stereoscopic camera drop reconstruction method in detail, starting from the image capturing and ending with the post processing of the measured drop profile.

3.1 Light Source

A key design consideration for constructing any optical measurement is selecting the proper light source and test surface. In this work, the light source must illuminate all areas of the drop without overexposure and create a speckle pattern when reflected from the sandblasted aluminum roughness samples.

Schmucker and White (2007) used a Helium-Neon laser to produce speckled images. Laser light is often used in speckled imaging as the collimated light from a coherent beam produces a speckled pattern from even slight surface roughness. The only requirement of the roughness is that the variations in surface height is larger than the wavelength of the laser (Briers 2007). The laser light hits the surface and reflects back to the camera lens but, due to the rough surface, the exact distance traveled from the laser source to the camera is slightly different at each point in the image. This causes a change in the phase of the beam which, when summed together on a camera's photosensor, creates areas of constructive and destructive interference. Laser speckle is highly sensitive to the initial conditions and any variations in the testing conditions can prevent the correlation of speckled patterns. The speckled pattern seen by the camera is dependent on the surface, the light source, and the viewing platform. Schmucker and White (2007) used a laser with a DC power source to eliminate any variations in the light source, but any movement of the camera such as vibrations caused by wind tunnel movement could affect the quality of the correlation.

Speckled images can also be captured using white light. While incoherent light sources do not produce the same speckled pattern produced by lasers, the resulting speckle fields are similar. Surface roughness features that are larger than the light's wavelengths create areas of light and dark pixels on an image that are spatially dependent and random. Schmucker and White (2012) used white light to capture speckle images as the laser illuminated data was more difficult to capture and did not produce higher quality

16

results.

Laser light was reconsidered in this work as the focused beam of laser light is very intense and could potentially increase the depth of focus of the camera lenses by reducing the required aperture diameter. Laser light also significantly reduces the reflection created by the light source reflecting off the drop interface. As there are advantages and disadvantages to each light source, laser light and white light speckle images were taken for the aluminum plated described above to determine which light source would be best for a stereoscopic experiment. A 5 mW 523 nm laser was used to test laser illumination for speckled images. Figure 3.1 below shows the laser creating a speckle pattern on the rough aluminum surface. The distinct areas of light and dark have very high contrast. Even with the camera aperture nearly closed, the bright peaks may oversaturate the image.
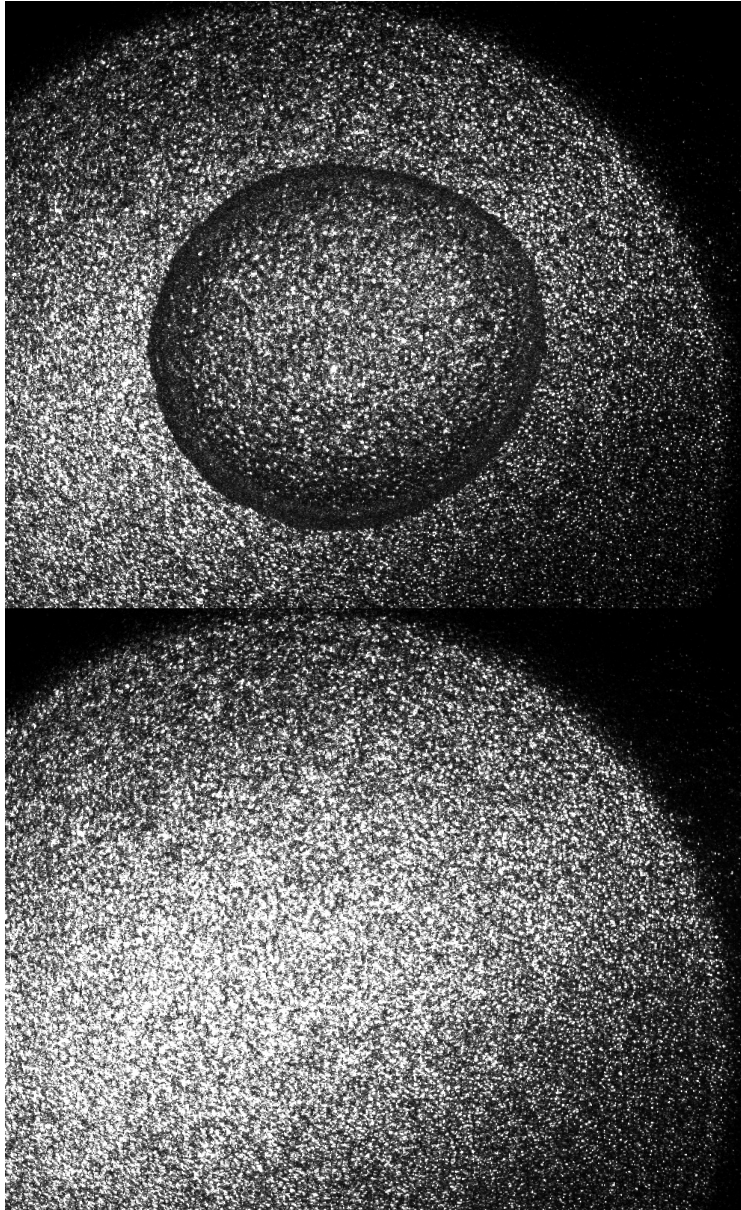
Figure 3.1: Sample drop (above) and control (below) images with laser illumination

Image oversaturation occurs when too much light hits the photosensor of the camera and the pixel intensity is captured as the maximum value. For an 8-bit grayscale image there are 256 intensity levels ranging from pure black with a value of zero to full white

with a value of 255. When the aperture is too large and the photosensor is flooded with light many of the pixels are assigned a value of 255. Conversely undersaturation occurs when not enough light is present and the image is too dark. The image correlation techniques explained below use the intensity values to determine pixel shifts. If the image is oversaturated too many pixels have the same intensity value. This hampers the ability of the correlation algorithms to relate the two images. Figure 3.2 shows a histogram of the drop image from Figure 3.1. The image is heavily oversaturated as the number of pure white pixels is an order of magnitude larger than any intermediate pixel level. Oversaturation cannot be fixed using image processing techniques as there is no data to extract even after balancing the image intensities histogram. Instead, it must be avoided prior to the image capture by decreasing the aperture or reducing the light intensity.

Laser light was found to be too difficult to balance for a wide range of drop images. Often, reducing the aperture to remove oversaturation reduced the amount of light captured around the edges of the drop. The edge region is particularly challenging because the light refracting nearest the edges of the drop experiences increased internal reflection which lowers the intensity of the reflected light significantly.
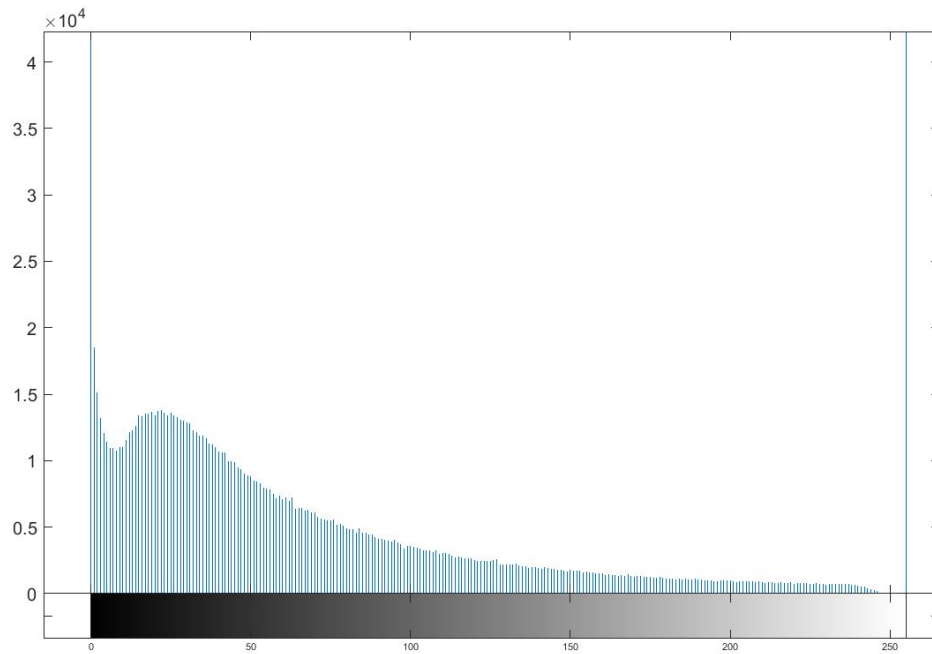
Figure 3.2: Histogram of laser illuminated drop image from Figure 3.1

Coming to the same conclusion as Schmucker and White (2012) from a different approach, white light was chosen to be the light source for the this work. White LEDs do not create the same high-contrast patterns as laser light, but the the surface roughness creates relatively lighter and darker areas as shown in Figure 3.3. White light also allows for multiple light sources to be used, as the grainy speckle pattern does not require a collimated light source to form. The light source used in Figure 3.3 was an LED ring light comprised of several discrete diodes.
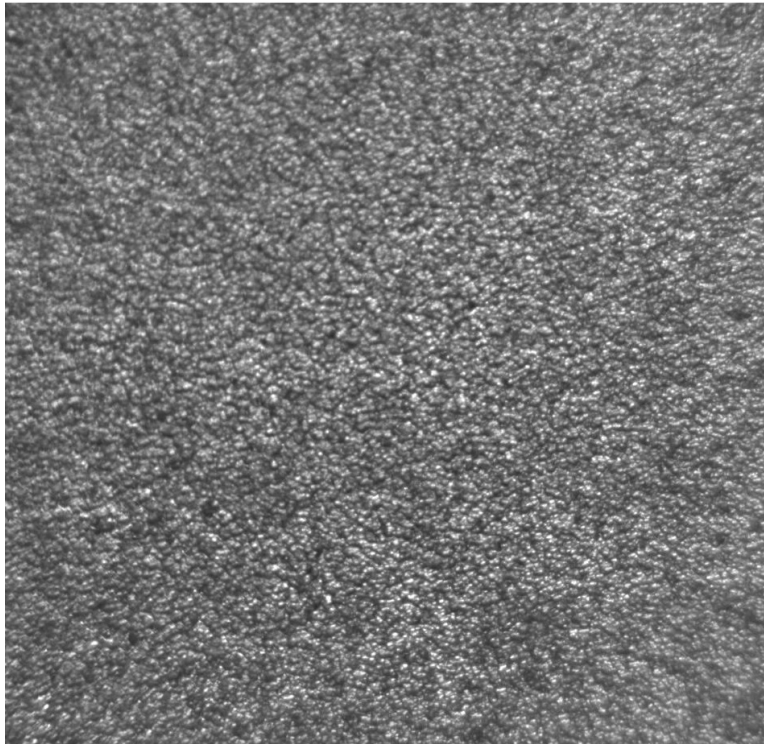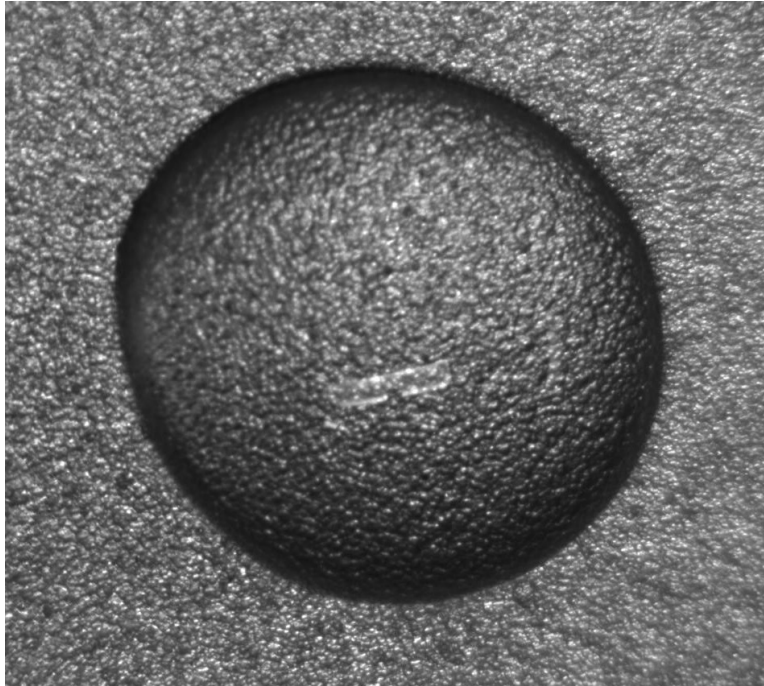
Figure 3.3: Sample drop (top) and control (below) images with white light illumination.

Figure 3.4 shows the histogram of the drop image from Figure 3.3. The histogram shows no oversaturated pixels and very few pure black pixels. The overwhelming majority of pixels in the image have an intensity value between 0 and 255, so every image subregion in the image can be successfully correlated with the surrounding pixels. Compared to the histogram in Figure 3.2, the laser light gives a more even distribution of pixel intensities than white light. However for the purposes of this experiment, avoiding saturated pixel intensities is more important than the overall distribution of intensities.
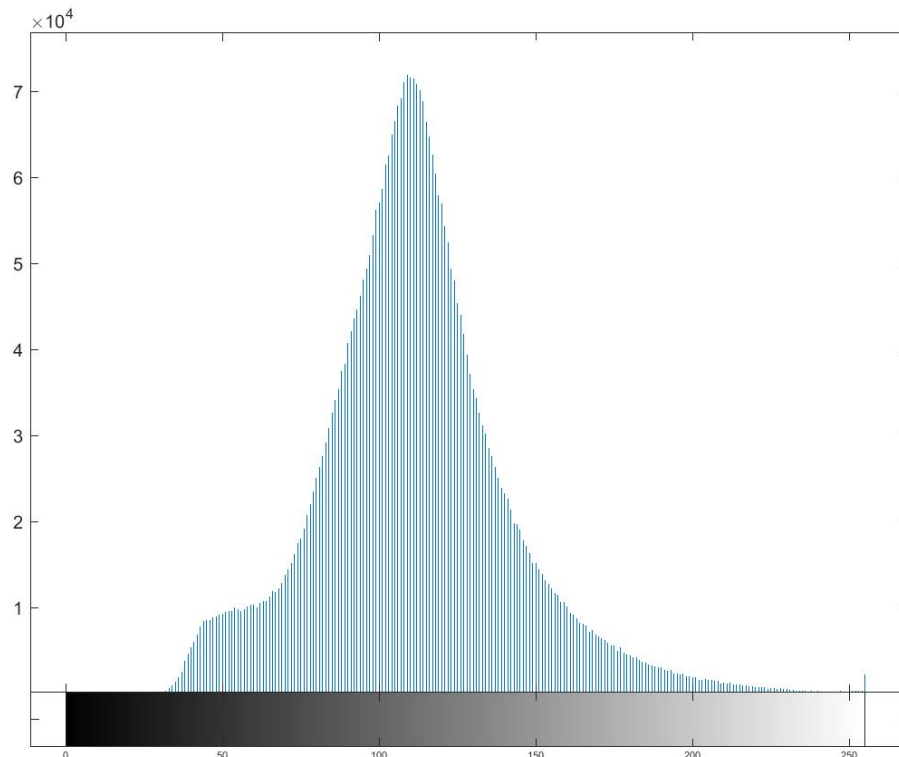
Figure 3.4: Histogram of white light illuminated drop image from Figure 3.3.

The main drawback of using a white light source is the specular reflection of the light source from the surface of the drop. If the light source is not diffused over a large enough

area or placed too close to the drop surface, the image will include the reflection of the light source as a bright spot. This reflection comes from the air/water interface and not the aluminum surface so only occurs in the drop images, not the control images. This can lead to issues correlating the surface speckle patterns between the two images.

Figure 3.5 shows the calculated z-direction speckle shift for a drop with three large areas of specular reflection. The data is lost not only at the pixels directly covered by reflections but also in the surrounding areas. The image subsample radius is set to 33 pixels, so any pixel within 66 pixels of a reflection may be unusable in the drop shift reconstruction methods. The reflection error is not unique to white light as laser light sources also show reflections off the drop surface, however the laser beam diameter is on the order of millimeters wide. This creates a much smaller area of specular reflection that can largely be ignored. To fix this issue, a larger LED panel was used with a light diffuser. By spreading the light source over a larger area, the average reflection intensity was reduced and does not oversaturate the underlying pixels. This allows the image correlation methods to match the speckle patterns as the pixel intensity variations are captured accurately.
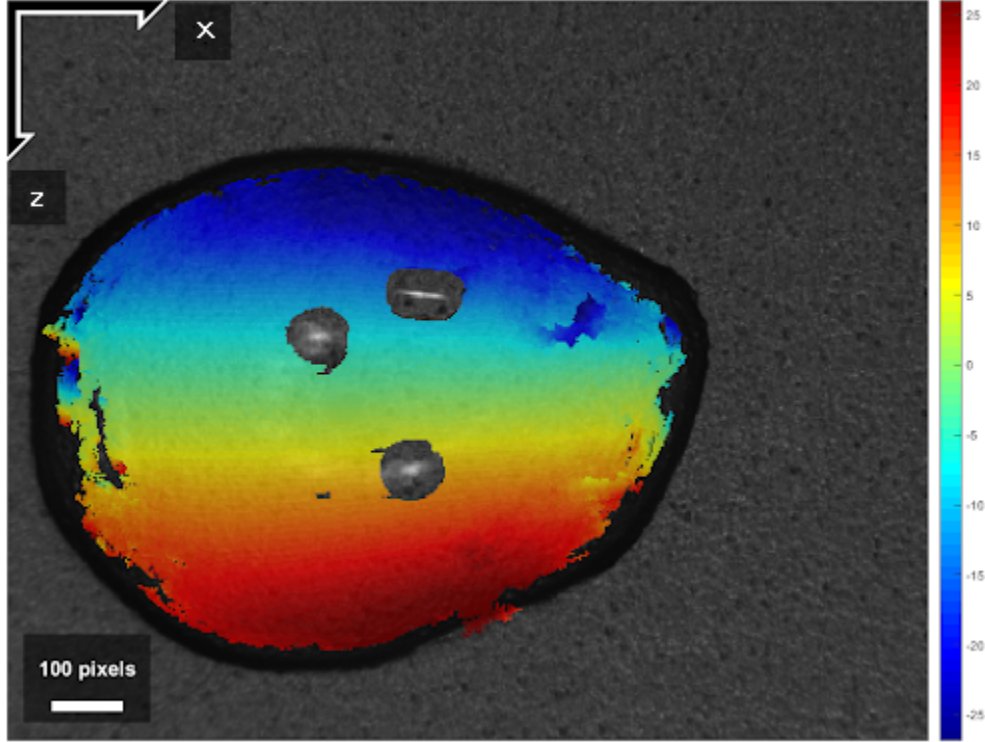
Figure 3.5: Sample z-direction speckle shift with specular surface reflection

3.2 Image Capturing

After choosing white light as a light source, the next experimental decision was to chose camera tilt angles. The tilt angle θ_c is defined from the vertical with $\theta_c = 0$ corresponding to the camera image plane parallel to the test surface. When the camera lens is angled from the receding side of the drop (uphill or upstream) θ_c is defined as positive. Conversely, θ_c is negative when tilted from downhill (or downstream) on the advancing side. For a setup with only a single camera, such as the work done by Schmucker and White (2007), a single camera with $\theta_c = 0$ was used exclusively.

The maximum possible value for θ_c is limited by the requirement that both inclined cameras be able to observe the entire contact line. This limited the maximum tilt angle

to 20°. This limit is also enforced by depth of focus considerations. When $\theta_c = 0°$, the camera can focus on the entire surface because the image plane is parallel to the test surface. When the camera is tilted, however, it is not always possible to have the entire drop in focus as it must be for successful speckle shift measurements.

The depth of focus of an optical system is the distance measured along the optical axis in which good focus can be achieved. In practical terms, it determines the range of distances the object in focus needs to stay within to remain in focus. The depth of focus is affected by the camera aperture diameter. As the aperture is closed the depth of focus is increased but less light is allowed into the camera. A delicate balance is formed between increasing the depth of focus while passing through enough light to properly view the speckle pattern. As mentioned previously, laser illumination was considered due to the intensity of the light allowing for a very small aperture. However, the increase in image quality using laser illumination was not significant enough to be useful. Scheimpflug adaptors can be used to align the image plane with the surface when cameras are inclined. But, by limiting the camera angles to small angles, these are not needed.

To select an optimum θ_c, images were taken for drops ranging from 50 to 200 μL and tilt angles from 0° to 20°. As shown in Figure 3.6 the depth of focus of the image begins to reach the edges of the drop when $\theta_c = \pm 15°$ and by $\theta_c = 20°$ parts of the drop are no longer in focus. To accommodate the largest possible θ_c, the cameras were adjusted to just focus on the advancing half of the drop or on the receding half. As long as the cameras have overlapping areas of focus in the center of the drop the reconstruction method has enough data to function properly. If the contact line is out of focus, however, the edge detection method can break down and the contact line cannot be guaranteed to be correct. This can be mitigated through manual correction, as described below for the case of $\theta_c = \theta_r$. Ultimately, tilt angles of $\pm 13°$ were chosen as the optimal configuration

to avoid that issue. A slight decrease from the maximum allowable tilt angle gives some margin of error for drops that exceed the limits of the tested drops.
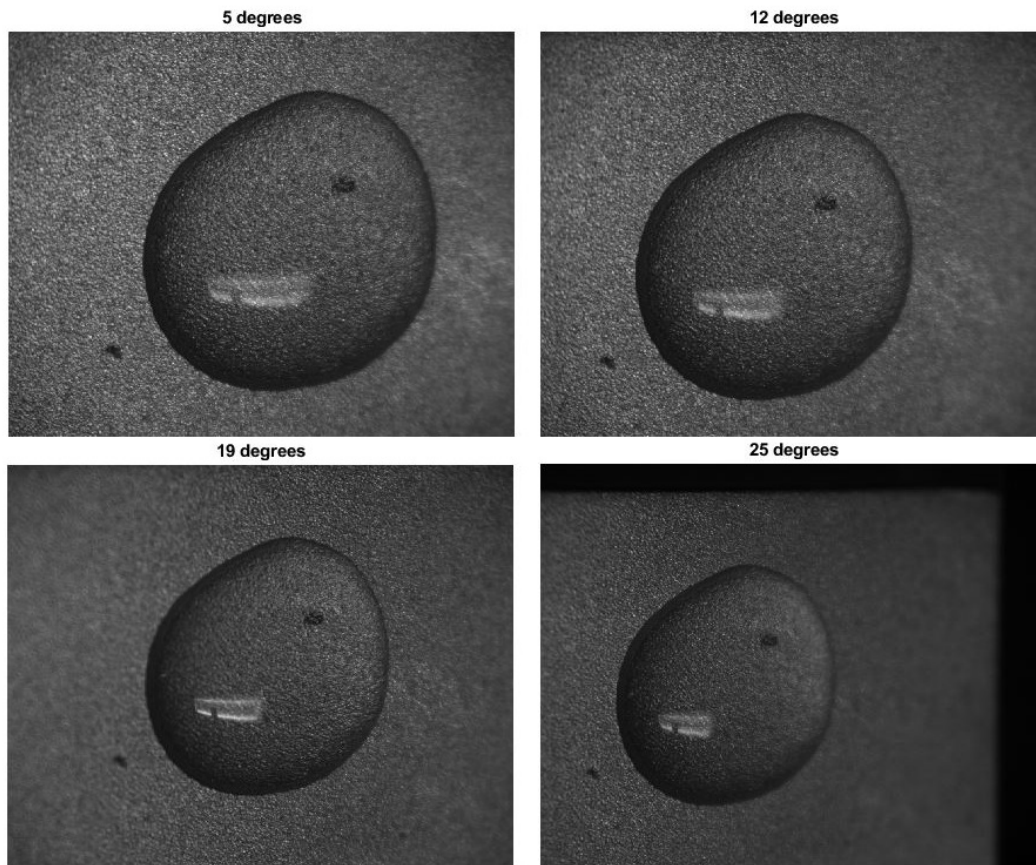

Figure 3.6: Sample drop imaged at various camera tilt angles.

3.3 Drop Reconstruction

3.3.1 Contact Line Detection

Once speckle images are collected, drop reconstruction analysis can begin. The first step is to find the contact line between the drop and surface. The accuracy of the contact

line is paramount as previous studies, such as Milne and Amirfazli (2009) and Dussan V. and Chow (1983), relate drop pinning force to contact line evolution as well as contact angle hysteresis. There are many varying approaches to edge detection in images, including pixel intensity gradients and variations. However, for speckled images, gradients change rapidly everywhere so a more specialized technique is required. The image could be blurred with a Gaussian kernel, but with blurring such large, discrete noise caused by the surface roughness the fidelity of the estimated edge is not guaranteed. Instead, the present method follows the steps outlined in Schmucker and White (2007) by subtracting the drop image from the control image to determine the contact line. The camera remains stationary between photos, so any difference in pixel intensities arises from the drop's presence. The image subtraction is then thresholded into a binary image based on the pixel intensity histogram, where a value of 1 represents a drop is present in that pixel and 0 being there is not a drop. The threshold value is not perfect because reflections created by the drop liquid can lead to false positives outside of the drop contact line.

A series of morphological opening filters scripted in Matlab are used on the binarized image to remove noise. An opening filter removes small objects from the foreground of a binarized image (value 1) and places them in the background (value 0). The first filter uses an 'island' structuring element which removes (set to 0) any value 1 pixels that are isolated from other value 1 pixels. This is from the assumption that the noise will be small and separate from the drop. A ring of 30 pixels across is sampled around each drop pixel and, if no other value 1 pixels are found in the ring, the sample pixel is determined to be noise. The process is repeated for a ring of 15 pixels across to remove smaller clusters of noise that may be in close proximity to one another. The final filter uses a square structuring element to remove any noise touching the drop profile itself. The morphological filters result in a binary image of only drop pixels. The edges of the

image are taken as (x, z) points and the resulting line is locally smoothed with a 5-point moving average. The final contact line is given in pixel coordinates and can be plotted on the original drop image as seen in Figure 3.7.
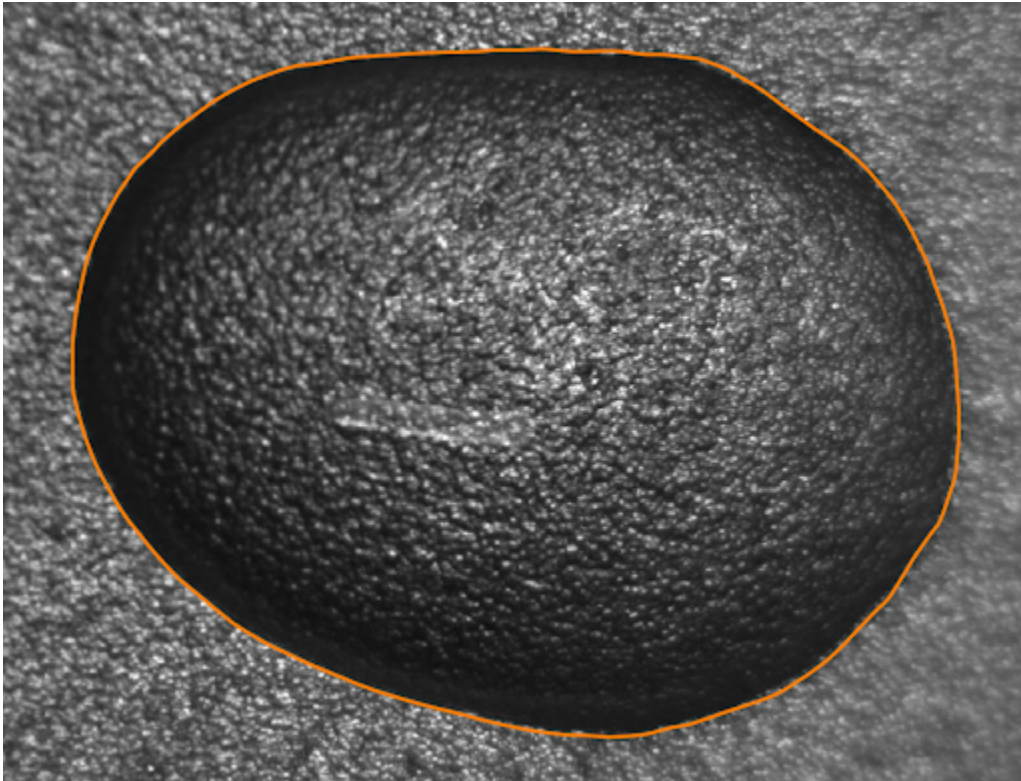
Figure 3.7: Sample drop image with calculated contact line

A potential issue occurs when the receding camera tilt angle exactly matches the slope of the drop at the receding contact edge. As shown in Equation 3.5 the pixel shift vector measured between the control image and the drop image is a function of the drop normal direction at that location. When a camera is tilted in the stereoscopic measurements, the angle the camera makes with the vertical can equal the receding contact angle. In this situation, the pixels are not shifted by the presence of the drop because the optical

axis is aligned with the interface normal direction. The contact line detection methods determine any pixels with zero shift to be background surface pixels. For Schmucker and White (2007) zero shift points occured at the drop apex inside the drop perimeter and hole-filling procedures or outermost edge segmentation finds the drop contact line without issue. However, if the drop slope at the contact line equals the camera tilt angle, as seen in Figure 3.8, the edge detection algorithm fails and a portion of the contact line is lost. While this is not common, larger drops and drops near deppining can have a receding contact angles between 10° and 20°. To remedy this issue, a manual selection tool was implemented. A few points (2 to 5) are selected along the contact line where the edge detection algorithm fails and those points are treated as known drop locations. The edge segmentation method is then able to fully capture the drop shape as normal.
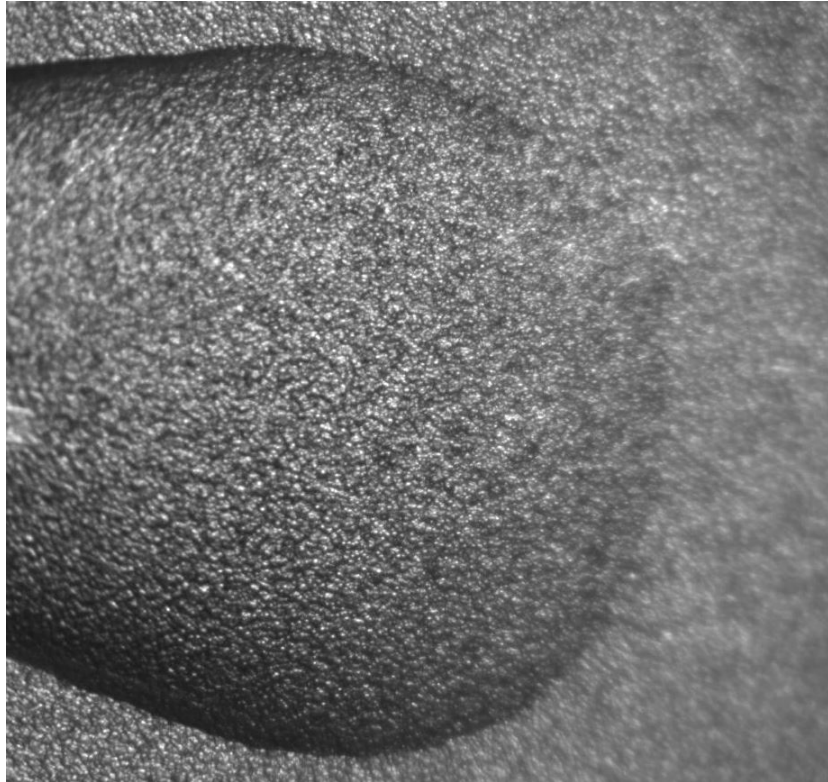
Figure 3.8: Drop with a receding contact angle close to θ_c.

The contact line is separately calculated for the advancing and receding cameras using the steps outlined above. Then, to relate the separate contact lines to each other, the four extrema are used: smallest x, smallest z, largest x, and largest z coordinates and the images are scaled to match these points. Figure 3.9 shows the calculated contact lines scaled in the streamwise x direction. As shown, the edge detection algorithm captures the same drop shape with both cameras regardless of camera angle.

The four scaling points must be visible to both cameras. Imaging a drop with an increasing contact angle hysteresis there is a point where the advancing contact angle becomes too large and obscures the position of the contact edge. This critical angle is relative to the camera tilt angle θ_c by $\theta_A = 90° - \theta_c$. It may be more useful to find the

maximum allowable camera tilt angle from the expected maximum advancing contact angle. The target range for stereoscopic camera measurements was determined to be for drops with less than 70° advancing contact angles, which allows up to 20° of allowable advancing camera tilt. For this experiment the limiting factor in determining camera tilt angle was not contact edge visibility rather the limits of keeping the drop in focus. A chosen camera tilt angle of ±13° allows the setup to effectively capture drops with advancing contact angles of up to 76.5°.
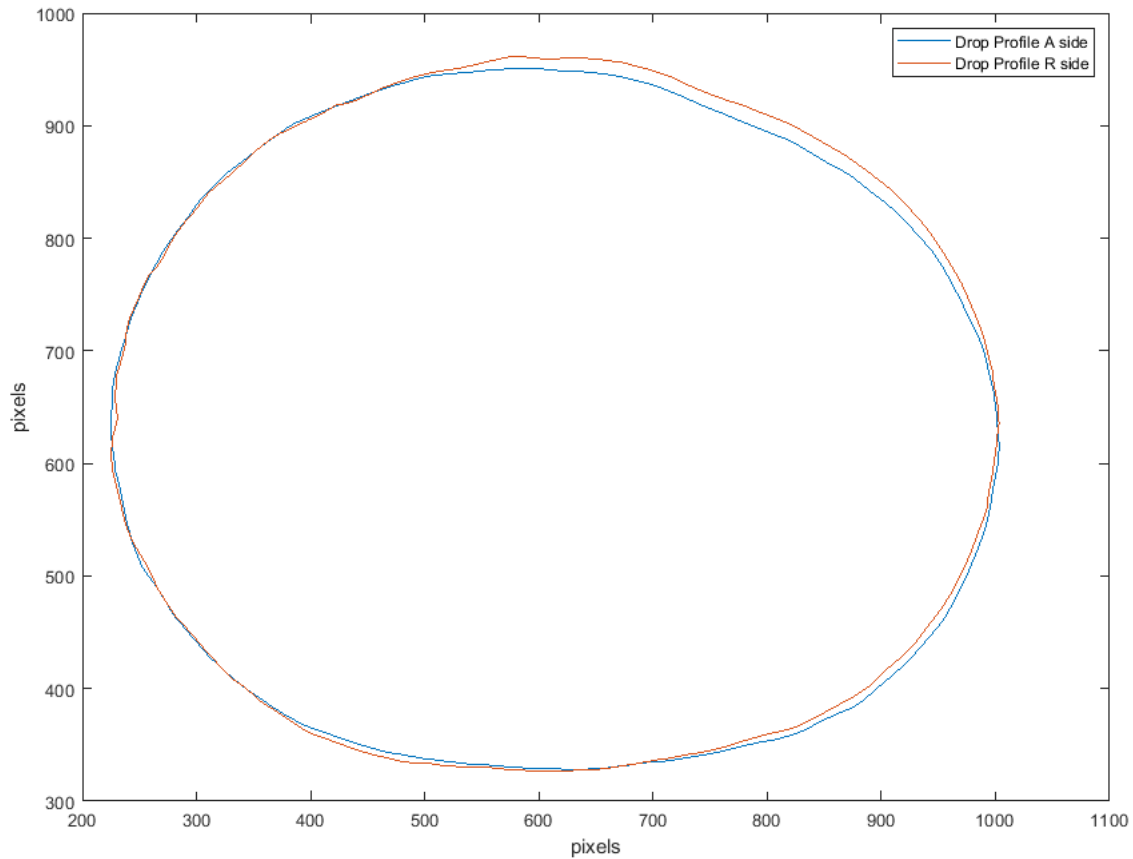

Figure 3.9: Advancing and receding contact lines scaled in x direction.

31

The drop contact line is used to map the advancing and receding cameras to each other, but each camera must then be calibrated to the physical domain. The calculations for the drop profile are performed in pixel coordinates, while the drop profiles must be returned in physical dimensions. Stereoscopic camera measurements in different fields often use a reference grid to calibrate the two cameras. Images are taken of a 2D surface, usually a black and white checkerboard pattern with known measurements, and a physical relationship is calculated between the two cameras. As many stereoscopic cameras are used in computer vision applications, the images are processed in real time and therefore require the calibration to be performed in advance of the image processing. The cameras must also stay static relative to each other from that point forward in the experiment when using a calibration grid which is cumbersome with the amount of minute adjustments made to the framing, zoom, and focus of the cameras during drop experiments. For this research images of a ruler are taken with both the advancing and receding cameras after each run is completed. Scale markers are identified manually and a pixel-to-inch scale is stored for the remainder of the data processing. By taking the calibration images at the end of each experiment, the camera configuration is guaranteed to match the drop and calibration images exactly.

3.3.2 Speckle Shift Measurement

After the drop contact line is located, analysis of the speckle patterns inside the drop begins. These shifts are a function of the interface height and slope and are the key input data of drop shape reconstruction. Schmucker and White (2007) measured $\vec{s}(x, z)$, the speckle shift field, using a cross-correlation method between the control and drop images. Square subregions were taken from the drop image around grid points x and z and correlations between the grayscale pixel intensities $f(x, z)$ in the chosen subregion and subregions in the control image. The correlation coefficient, which describes how

well the two subregions match is

$$C_c = \frac{\sum_{(j,k)}(f_c(x_c, z_c) - \bar{f}_c)(f_d(x_d, z_d) - \bar{f}_d)}{\sqrt{\sum_{(j,k)}(f_c(x_c, z_c) - \bar{f}_c)^2 \sum_{(j,k)}(f_d(x_d, z_d) - \bar{f}_d)^2}} \tag{3.1}$$

where the subscripts c and d correspond to the control and drop images, respectively. The average grayscale pixel values in the subregions are $\bar{f}$. The (i, j) subscripts represent the grid nodes that map the inner area of the drop. By subtracting from the average intensity, the effect of differences in total brightness between the two images is reduced. This is necessary as the speckle pattern when refracted through the drop interface has a slightly lower average intensity due to luminance lost to internal reflection. The loss in refracted intensity is exponential approaching the edge of the drop, which may make it harder to analyze subregions near the contact line where the brightness variations may not be uniform. The correlation coefficient was computed for each potential shift between the two images. Schmucker and White (2007) achieved sub-pixel accuracy using a Gaussian distribution about the lowest correlation point.
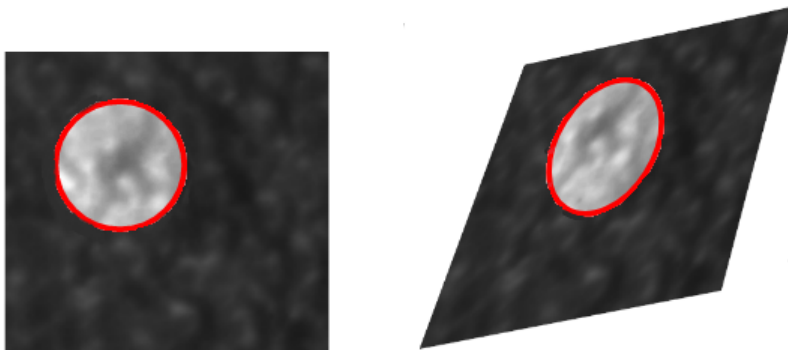

Figure 3.10: Speckle field deformation

33

For the present work an open-source correlation code was used instead of locally developed software. The program is NCorr, an open source Digital Image Correlation (DIC) program developed by Blaber et al. (2015). NCorr has been thoroughly tested and is natively interfaced in Matlab so easily integrates with the rest of the image processing methods. Structural DIC measurements, for which NCorr was created, utilize artificial speckle patterns on solid materials to measure in plane strains using speckle shift measurements. Although the refraction through a water drop is different, the image correlation methods are the same. NCorr starts by taking a rectangular subwindow of pixels about the drop and only calculates shift measurements for pixels inside. This significantly reduces the calculation time by ignoring areas of the image with only background pixels. It is also possible to use the binary drop area image from the edge detection procedure as a subwindow to minimize computation time, but this risks missing pixels very near the contact line due to the smoothing of the drop edge. Then a seed point is input to the program GUI. The seed point acts as an initial guess for the shift vector of surrounding pixels, and so is the only pixel in the analysis to not have an informed guess on the shift field (Blaber et al., 2015). The process described below is performed for the seed point, and if no converged shift value is found the process fails and a new seed is selected. The seed is often in the center of the drop where the pixel shifts are smallest to minimize the number of iterations required to converge on a solution. The seed is selected in the center for Figure 3.11 and, as the subregion only deforms slightly, only 13 iterations are needed for convergence.
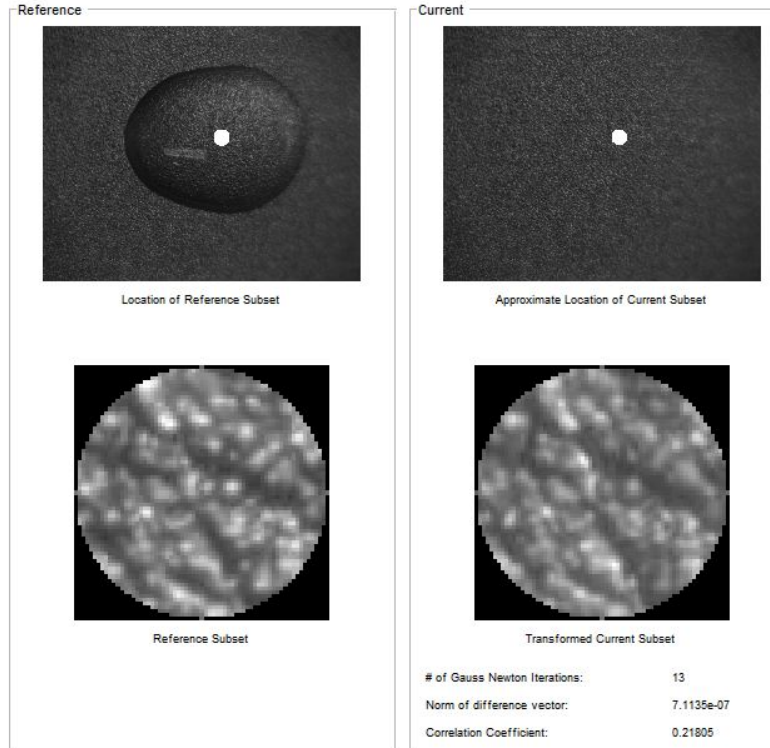
Figure 3.11: Seed placement and initial calculation

As the shift field is continuous, not every pixel in the drop area is calculated over. A sampling frequency, usually every third pixel, is used to speed up the computation without compromising the fidelity of the results. Pixels adjacent to the seed point are chosen first using an adjacent pixel shift as an initial guess for the shift vector. The initial guess is then input into an inverse compositional Gauss-Newton optimizer method. The optimizer solves for the pixel shifts, u and v, but also the pixel gradients $du/dx, du/dx, du/dx$ and dv/dz (Blaber et al., 2015). The pixel gradients deform the subregion to best fit the deformed speckle field as shown in Figure 3.10 above. Up to one hundred Gauss-Newton iterations can be performed per pixel but, for the majority of drop images, fifty iterations is sufficient. The iteration count can be increased after manual inspection of the

35

shift deformation field reveals an incorrect solution. The process repeats until all sampled pixels in the image have solutions. The final resulting shift field is shown in Figure 3.12 below. Scalar shift components u and v are shown separately, together they comprise the shift vector field $\overrightarrow{s}(x, z)$.
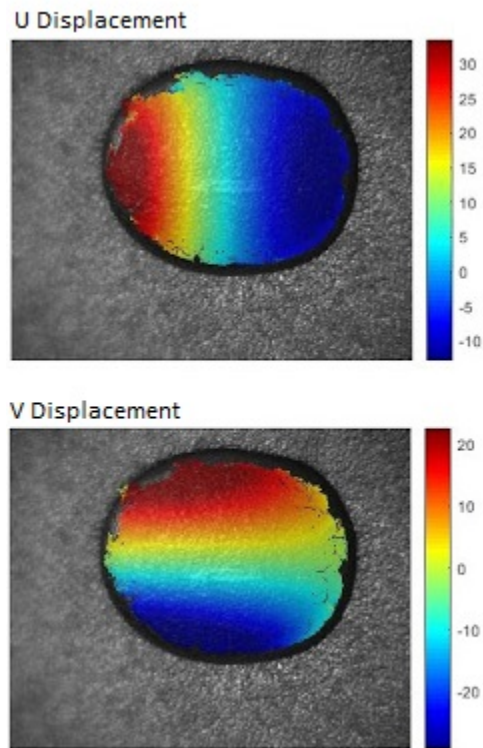
Figure 3.12: Shift vector components in u (left) and v (right). Contour color scale is pixels of displacement

In addition to the $\overrightarrow{s}(x, z)$ results, NCorr provides correlation scores that measure of how closely the pixel intensities from the undeformed subregion in the control image match the pixel intensities from the deformed subregion in the drop image. An example of the correlation scores for a completed DIC analysis is shown below in Figure 3.13,

scaled from 0 to 2.5. Different from the usual definition of correlation score given above, lower scores correspond to a higher confidence in the accuracy of the calculated shift vector. Scores greater than 1.5 are likely to be spurious and scores greater than 2 are almost guaranteed to be spurious. It is important to note that the correlation score is not an estimation of the measurement error, but a rather a measure of confidence in the accuracy of the answer. Figure 3.13 also shows how two cameras capturing different data sets over the same drop is beneficial, as often grid locations that are not correlated well (or at all) in one image are captured with confidence in the other. This usually occurs near the contact line where the surface slope is large and image contrast is lowest.
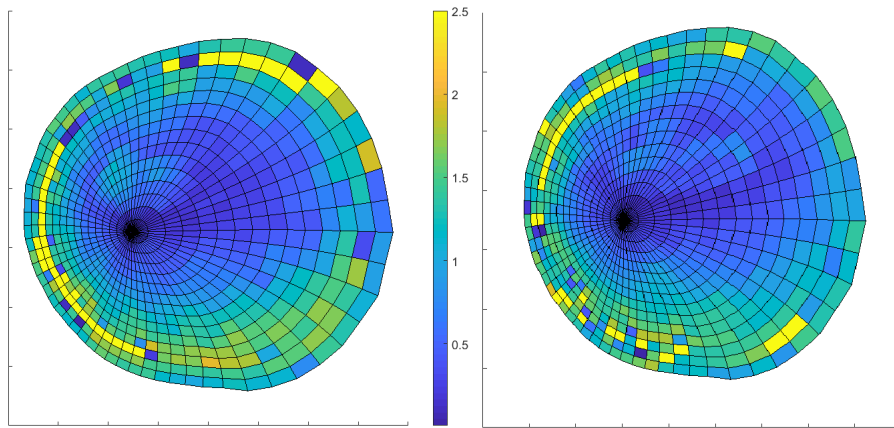
Figure 3.13: Scaled correlation scores for both advancing (left) and receding (right) shift measurements

The shift vectors output by the DIC process are not always correct. The erroneous shift vectors can hamper the reconstruction. This is especially true around the very edges of the contact line where the speckle pattern is barely visible, as the measured shifts at a few locations can change direction implying an inflection point in the drop profile which cannot be physical. To remove the spurious vectors from the data, each (u, v) pair is

compared to the magnitude of the vectors surrounding it and the direction of the other shifts along the same grid line. Measured data is flagged as a potential outlier if either the magnitude or direction is greater than one standard deviation away from the average of the surrounding vectors along the same grid line. This process can potentially have a high false positive rate for flagging data, especially for highly-forced drops with large changes in surface slope. However with two cameras each gathering DIC data over the drop, there exists more than enough data to complete the reconstruction even when some non-spurious shift vectors are removed.

3.3.3 Grid Generation

Drop reconstruction is performed using a set of basis functions defined on the unit disk. To enable this, the drop perimeter must be mapped to the unit circle and interior points to points in the unit disk. This is done using a set of radial/circumferential grid lines on the unit disk that are mapped to physical (x, z) coordinates. To begin, the center of the grid is defined. The drop area center can be used but, for drops with non-circular contact lines, the optimal grid center is usually not the centroid. Instead, mapping the center of the grid to the tallest point on the drop provides a strong initial guess of the drop profile which minimizes the optimization effort required to converge on the correct drop solution.

Using a single overhead camera, Schmucker and White (2007) found the drop apex in a straightforward way. Equation 1.2 for the shift vector $\overrightarrow{s}(x, z)$ with no camera tilt depends on the $\tan^{-1}(\nabla y)$. At the highest point on the drop the surface slope is zero, and so the shift vector is zero as well. The grid center location is simply the location of the smallest shift vector in the drop area. When the camera is tilted the process of finding the grid center becomes more difficult. As the cameras are tilted, there is still a measured shift when the surface slope becomes zero there. Therefore, to find the drop apex, the

shift vector fields of both the advancing and receding images are added together. If the two camera angles are equal and opposite, the shift vectors at the apex will be equal and opposite so the minimum of the summed shift vector field is chosen to be the grid center. Figure 3.14 below shows the advancing and receding shift fields and resultant sum of the advancing and receding shift vectors. The center of the grid is marked with the yellow square.

Once the grid center is located, an initial algebraic grid is generated using a set of straight radial lines in (x, z) space, evenly spaced in the circumferential direction. A set of J circumferential lines cross the radial lines at fixed fractions of the radial lines' lengths. The last of these lines $j = J$ is the drop's contact line. The center is $j = 0$. Working from the algebraic grid, an elliptic grid is generated. The elliptic grid retains the center point and radial line intersections with the contact line of the original algebraic grid. However, the elliptic grid requires that the radial and circumferential lines are mutually perpendicular is $(x.z)$ space as they are in the unit disk. This is particularly useful as the contact line where the contact angle is defined in the direction perpendicular to the contact line.
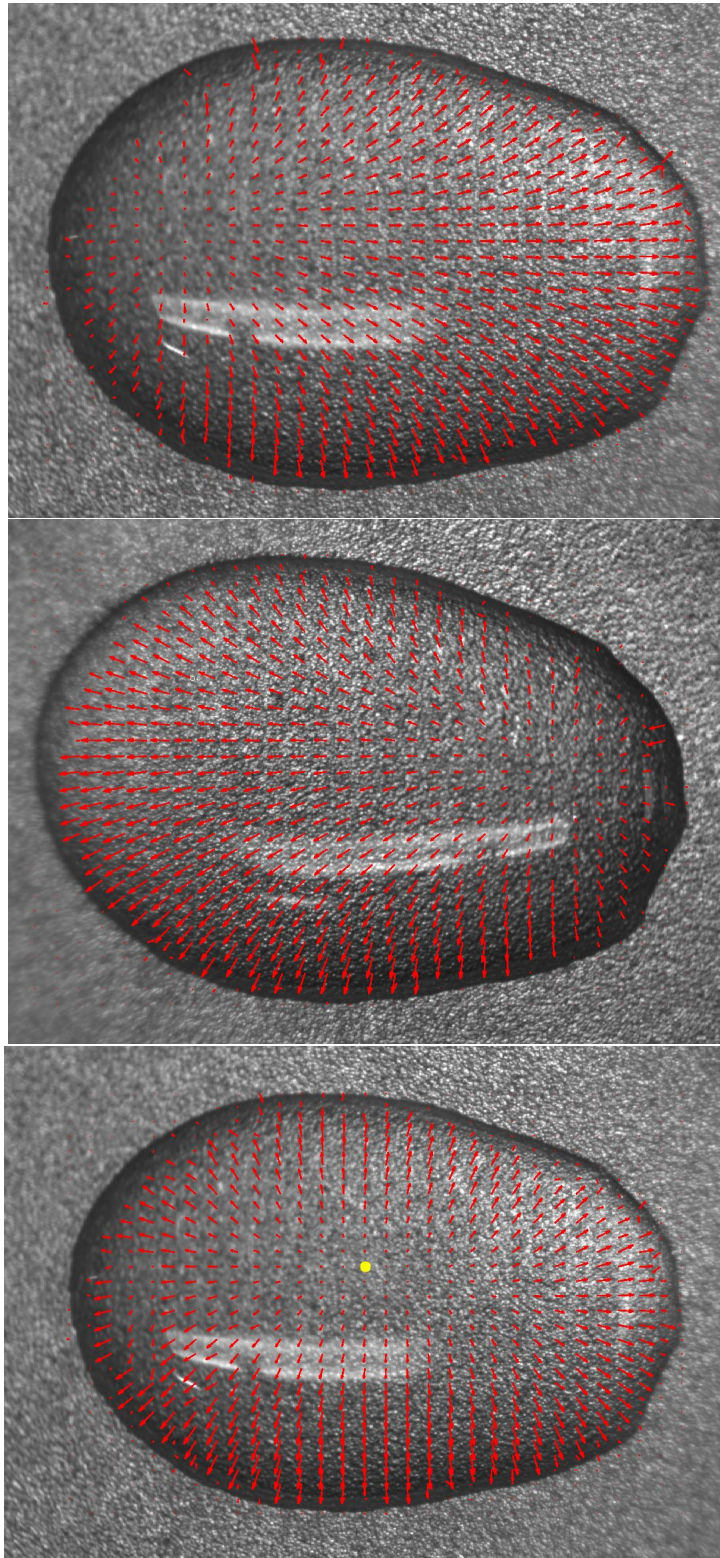
Figure 3.14: Sum (bottom) of advancing (top) and receding (middle) shift vector fields
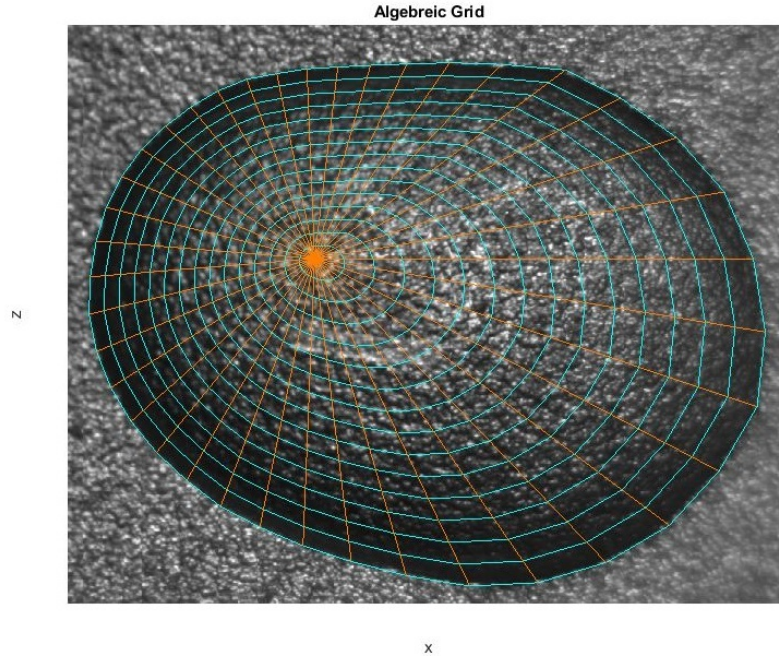
Figure 3.15: Grid shown with computational domain and algebraic grid.

The elliptic grid is generated by requiring the grid coordinates be solutions to Laplace's Equation:

$$\nabla^2 \zeta = 0$$
$$\nabla^2 \eta = 0$$

(3.2)

where ζ and η are the grid coordinates in the computational domain and $x(\zeta, \eta)$ and $z(\zeta, \eta)$ are the grid coordinates in the spacial (image) domain. Laplace's equation must be inverted because $x(\zeta, \eta)$ and $z(\zeta, \eta)$ are the desired results in the computational domain. The transformation from the physical to computational space results in:

$$\alpha x_{\zeta\zeta} - 2\beta x_{\zeta\eta} + \gamma x_{\eta\eta} = 0$$
$$\alpha z_{\zeta\zeta} - 2\beta z_{\zeta\eta} + \gamma z_{\eta\eta} = 0$$

(3.3)

41

where

$$\alpha = x_\eta^2 + z_\eta^2$$

$$\beta = x_\zeta x_\eta + z_\zeta z_\eta \qquad (3.4)$$

$$\gamma = x_\zeta^2 + z_\zeta^2$$

Both expressions from Equation 3.3 are solved simultaneously using an iterative numerical method. A converged elliptic grid is shown in Figure 3.16 below. Even with an irregularly shaped drop, as desired the grid lines are mutually perpendicular to the contact line and are evenly spaced in the radial direction.

Figure 3.16: Converged elliptic grid superimposed on advancing drop image.

3.3.4 Calculating Reconstructed Speckle Shifts

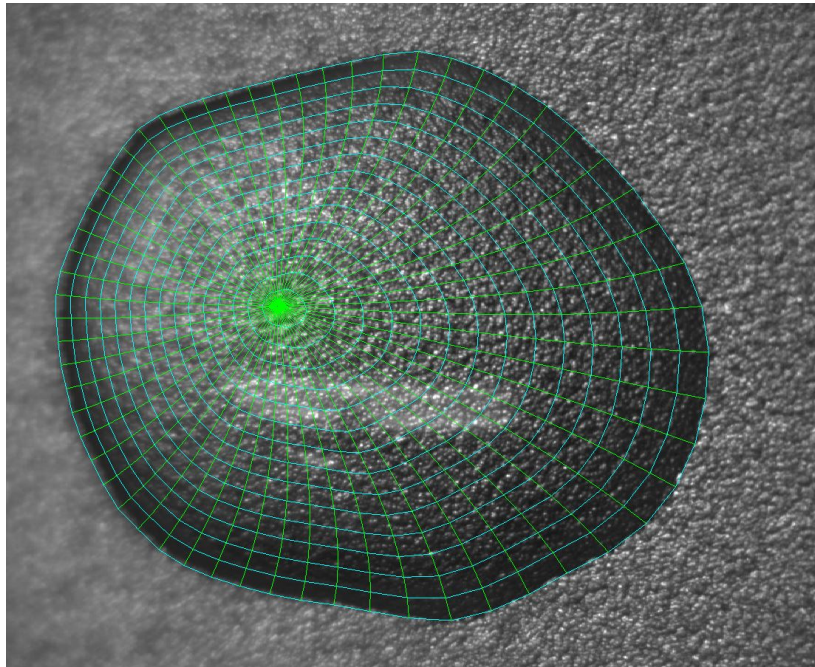With an assumed drop profile and the shift vectors extracted from the DIC analysis, the reconstruction process can begin. Candidate drop profiles, specified as $y(x, z)$ drop heights, compare what their shift vectors would be to the measured shift vector field for both the advancing and receding images simultaneously. This allows an optimization procedure to minimize the error between the shift fields by changing the $y(x, z)$ points. However this requires a complex ray tracing analysis to calculate the shift vector field from a candidate profile.

When no water drop is present, the ray from a surface point $\overrightarrow{p}$ reaches the inclined camera along ray $\overrightarrow{u}_0$. This vector is parallel to the camera's axis, which is a function of the camera angle $\overrightarrow{\theta_c} = (\theta_c^x, 0, \theta_c^z)$. The camera angles θ_c^x and θ_c^z are defined as a positive rotation about the z and x axis respectively. Note that previously $\theta_c = \theta_c^x$ as the z component is very small and only influences the ray tracing calculations. The vector that describes the camera's axis is $\overrightarrow{u}_0$ and is found by rotating the vertical camera axis by θ_c^x and θ_c^z.

When a drop covers point $\overrightarrow{p}$, the ray that reaches the camera travels along ray $\overrightarrow{u}_p$, refracts across the inclined interface at point $\overrightarrow{x} = (x, y, z)$, then continues to the camera along refracted ray $\overrightarrow{u}_r$ that is parallel to $\overrightarrow{u}_0$. From the perspective of the camera, the ray $\overrightarrow{u}_r$ appears to have originated at surface point $\overrightarrow{a}$ and to have traveled along ray $\overrightarrow{u}_a$ from the surface. That is, the speckle pattern on the surface at point $\overrightarrow{p}$ appears to shift by $\overrightarrow{s}$ to point $\overrightarrow{a}$.

Refraction is governed by Snell's law so $n_{water} \sin \theta_1 = n_{air} \sin \theta_2$ where n_{water} and n_{air} are the refractive indices of water and air, θ_1 is the angle between the surface normal vector $\overrightarrow{n}$, and $\overrightarrow{u}_p$ and θ_2 is the angle between $\overrightarrow{n}$ and $\overrightarrow{u}_r$ that must be parallel to $\overrightarrow{u}_0$ to be captured by the camera. The interface normal vector is $\overrightarrow{n} = (-\delta y/\delta x, 1, -\delta y/\delta z)$.

The refraction problem is complex because the interface can be inclined in both the x and z directions. This means the angles θ_1 and θ_2 are not measured in the plane of the figure. When ray $\vec{u}_p$ refracts across the interface, the refracted ray $\vec{u}_r$ must lie in the plane defined by $\vec{u}_p$ and $\vec{n}$. This constraint is expressed as $\hat{u}_r \cdot (\hat{u}_p \times \hat{n}) = 0$. The magnitudes of these vectors are irrelevant because the right-hand side is zero. Thus, $\vec{u}_r$ can be replaced with $\hat{u}_0$. Rearranging, this yields $\vec{u}_p \cdot \vec{b} = 0$ where $\vec{b} = \hat{u}_0 \times \vec{n}$.

The essence of the reconstruction method is to specify a camera inclination angle that sets $\vec{u}_0$ as a function of the camera inclination angle to measure $\vec{s}(\vec{p})$, a field of speckle-shift vectors originating from every point $\vec{p}$ inside the drop contact line. This data is used to calculate the interface shape, $y(x,z)$. This is a generalization of the method introduced by Schmucker and White (2007) that allows for non-zero θ_c values and the advantages this introduces. However, a complexity introduced by this generalization is that the point $\vec{x}$ on the interface through which ray refracts is not directly above point $\vec{a}$ so care must be taken to associate the correct data with points. Furthermore, the ray diagram cannot be drawn in a single plane for an arbitrary interface slope and this requires careful consideration of the constraint that refraction occur within the plane defined by $\hat{b} = \hat{u}_0 \times \hat{n}$.

The key questions is: "For a particular $\vec{p}$ and corresponding $\vec{s}$, what is $\vec{x} = (x, y, z)$?" The three components of $\vec{x}$ represent three unknowns but these can be quickly reduced to one. The $\vec{a}$ vector is known because $\vec{a} = \vec{p} + \vec{s}$. The interface position is given by $\vec{x} = \vec{a} + \vec{u}_a$. The apparent ray vector $\vec{u}_a$ is parallel to $\vec{u}_0$ so $\vec{u}_a = (1 - \tan \vec{\theta}_c) y$. The $\vec{x}$ components are not known independently but can be specified as a function of the interface height y. That is, there is only one unknown in corresponding to a particular and measurement.

The unknown interface height might be resolved using ray geometry. Ray $\vec{u}_p$ has

components (u_p, y, w_p) and $\vec{u}_p = \vec{s} = \vec{u}_a$. Considering components reveals $u_p = s_x - \tan\theta_c^x y$ and $w_p = s_z - \tan\theta_c^z y$ where s_x and s_z are the x and z components of $\vec{s}$. That is, $\vec{u}_p$ is also a function of the key unknown, y.

Snell's law and the planar refraction constraint might be used to find y. The angles in Snell's law are generated using $\cos\theta_1 = \hat{u}_p \cdot \hat{n}$ and $\cos\theta_2 = \hat{u}_0 \cdot \hat{n}$ where replacing $\rightarrow$ with $\hat{}$ signifies a unit-length vector in the same direction as the original vector. Again, the refraction must remain in the plane normal to $\hat{b} = \hat{u}_0 \times \hat{n}$ so $\vec{u}_p \cdot \hat{b} = 0$. In these equations, the interface slopes $\delta y/\delta x$ and $\delta y/\delta z$ are two additional unknowns in $\vec{n}$. That is, Snell's law and the planar refraction requirement are two additional constraints but introduce two additional unknowns. The problem cannot be closed so an inverse approach is needed. Figure 3.17 below shows the path the rays
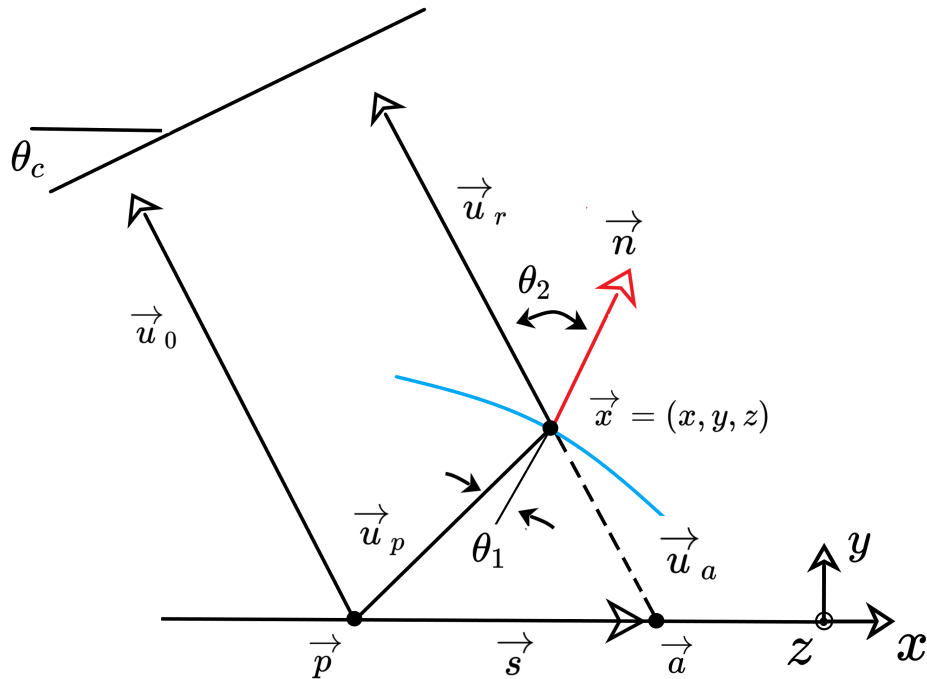

Figure 3.17: Speckle Shift Ray Tracing Diagram.

Interface reconstruction using an inverse method consists of specifying a candidate interface shape $y(x, z)$ and using that shape to calculate and the corresponding $\vec{s}(\vec{p})$ vector fields. This approach can succeed because the candidate interface shape also specifies the refraction location $\vec{x} = (x, y, z)$ and derivatives $\delta y/\delta x$ and $\delta y/\delta z$ that are needed for refraction calculations. The u_p and w_p components of $\vec{u}_p = [u_p, y, w_p]$ are found from the relations $\vec{u}_p \cdot \hat{b} = 0$ and $\cos\theta_1 = \hat{u}_p \cdot \hat{n}$.

As an algorithm.

1. Find the normal vector $\vec{n} = [-\delta y/\delta x, 1, -\delta y/\delta z]$ from the assumed drop interface $y(x, z)$

2. Find the camera inclination vector $\vec{u}_0$

3. From steps 1 and 2 find $\cos\theta_2 = \hat{u}_0 \cdot \hat{n}$

4. Solve the system of equations for the u_p and w_p components of $\vec{u}_p = [u_p, y, w_p]$ using the equations $\vec{u}_p \cdot \hat{b} = 0$ and $\cos\theta_1 = \hat{u}_p \cdot \hat{n}$ being careful of when unit vectors are needed

5. Using $\vec{u}_p$ calculate $\vec{s} = \vec{u}_p - \vec{u}_a$

This process is repeated for every grid node in the drop area and results in a shift vector field for the assumed interface shape $y(x, z)$. The shift vectors $\vec{s}(\vec{p})$ are then compared to the vectors found by the DIC program.

Solving the non-linear system of equations for $\vec{u}_p$ over hundreds of grid nodes is computationally expensive especially when repeated in an optimization loop. A simplification can be made to increase computation speed by making the assumption that the points $\vec{x}$ and $\vec{a}$ are directly above each other, that is $\vec{u}_a = [0, 1, 0]$. This significantly simplifies the problem and allows for an approach similar to Schmucker and White (2007). A beam

of light is traced through the air-water interface as it approaches an inclined camera lens as shown in Figure 3.17 above. Again the rays of light are traced from the surface without a drop present, $\overrightarrow{u}_0$, and with the drop present, $\overrightarrow{u}_r$. The drop normal is now defined by the surface height gradient, $\nabla y = (dy/dx, dy/dz)$, and makes the angle $\theta_1 = \tan^{-1}(\nabla y)$ from the vertical. This simplification allows using Snell's law to easily find θ_2 from the assumed drop shape $y(x, z)$. Subtracting the surface normal angle from the camera tilt angle θ_c gives the angle ray $\overrightarrow{u}_p$ must take to reach the camera lens. From this the estimated shift vector can be found by

$$\overrightarrow{s}(x, z) = \frac{-y\sin(\tan^{-1}|\nabla y|)) + \sin^{-1}(\frac{n_{air}}{n_{water}}\sin(\theta_c - \tan^{-1}(|\nabla y|))) - \theta_c)}{\cos(\tan^{-1}(|\nabla y|)) + \sin^{-1}(\frac{n_{air}}{n_{water}}\sin(\theta_c - \tan^{-1}(|\nabla y|)))} \frac{\nabla y}{|\nabla y|}$$

(3.5)

When the camera angle $\theta_c = 0$ Equation 3.5 reduces to Equation 1.2. This assumption is very close to the correct shift measurement as the x and z components of the $\overrightarrow{u}_a$ vector are often very small. As described below, the estimated shift vectors found in Equation 3.5 are a useful tool in accelerating convergence for the more correct non-linear solution.

3.3.5 Profile Reconstruction using Basis Functions

The reconstruction method relies on a representation of the drop height valid anywhere in the drop surface. As discussed above, the assumed drop solution $y(x, z)$ must also define the drop normal vector at every location as well. Schmucker and White (2007) do this using in a series of Fourier-Bessel functions and the same approach is used here. A summation of periodic functions provide a simple and workable basis for drop shape reconstruction with several inherent advantages. Firstly, by defining the drop radius as one period the contact line boundary condition of drop height $y = 0$ is automatically satisfied. The Fourier-Bessel modes are always smooth and differentiable, as all physical drop pro-

files are. Finally, and most importantly, the dimensionality of the reconstruction problem is reduced significantly. Instead of finding the drop height at each grid node, the drop profile can be represented by amplitude coefficients of basis functions. The Bessel functions are used in the form of $y(j,k) = \sum_{n=1}^{N} \sum_{m=-M}^{M} A_{-m,n} J_{-m}(\alpha_{m,n}j/J) \exp 2\pi imk/K$, where $A_{m,n}$ is the complex-valued amplitude, $\alpha_{m,n}$ is the nth real root of the mth-order Bessel function of the first kind, J_m. (Note that J_m is not to be confused with J, the total number of radial points on the elliptic grid). As m can be negative, the Bessel functions of a negative order are related to the positive order functions by $J_{-m} = (-1)^m J_m$. For y to be real-valued it is required that $A_{-m,n} = (-1)^m \bar{A}_{m,n}$ where the bar denotes the complex conjugate. Combining these two expression yields $A_{-m,n} J_{-m} = \bar{A}_{m,n} J_m$.

The basis functions can represent any drop shape with enough modes, however to minimize the amount of mode shapes needed a spherical cap mode is added as a '0th' order mode. The cap mode is often the largest mode in the reconstruction as many drops are generally spherical in nature and the basis functions can fine tune the resulting profile. The spherical cap is represented by a single coefficient A_{SC} and the final expression for the drop height is

$$
\begin{gathered}
y(j,k) = R_{max}(\sqrt{1-(j/J)^2} - A_{SC}) + ... \\
... + \sum_{n=1}^{N} \sum_{m=-M}^{M} A_{-m,n} J_{-m}(\alpha_{m,n}j/J) \exp 2\pi imk/K
\end{gathered}
\tag{3.6}
$$

where R_{max} is a constant defined as half of the length of the drop. R_{max} scales the spherical cap mode from the unit circle to pixel coordinates. Along with the spherical cap mode coefficient A_{SC}, the coefficients used to represent the drop shape are the complex amplitudes $A_{m,n}$. A standard drop profile reconstruction used $M = 3$ and $N = 3$, giving 10 total unknown coefficients. However as each amplitude is complex, the real and imaginary parts of the amplitude are handled separately giving 16 separate variables that

represent the drop shape. (Note the $M = 0$ Bessel amplitudes and the spherical cap coefficient A_{SC} are not complex).

3.4 Optimization

The basis functions and spherical cap mode amplitudes are determined using a non-linear optimizer. The algorithm searches over the design space to find an acceptable value for each coefficient. As with most frequency models, the most important coefficients are usually the lowest order modes the first Bessel mode J_0 and the spherical cap mode A_{SC}. The J_0 Bessel coefficient is generally negative which decreases the height of the spherical cap mode but increases the contact angles. This is due to the Bessel function of the 0_{th} kind being positively valued at 0, unlike any succeeding orders.

The optimization scheme used in this research was the Nelder-Mead method, also known as the downhill simplex method (Nelder and Mead, 1965). This numerical solver was selected as the derivatives of the objective function are unknown and the design space is N dimensional, where N is the number of real-valued Bessel and spherical cap coefficients used in the reconstruction. The Nelder-Mead method is a heuristic search and uses the geometric concept of a simplex, which is a polytope shape with $N + 1$ vertices in N dimensions. The objective function required for the algorithm may be non linear but must vary smoothly, which the error function χ^2 in Equation 3.6 below. The algorithm starts with the first vertex, an initial guess of the drop profile, which is the J_0 Bessel coefficient and the A_{SC} and small random non-zero components for the rest of the coefficients. By starting with the largest contributors to the drop shape, a physical solution is generally found sooner as the resulting drop profiles usually result in the spherical cap mode and J_0 Bessel mode dominating the other Bessel modes.

The Nelder-Mead method is efficient and does not add randomness into the design variables. However, the algorithm may converge to a sub-optimal solution. Without

adding random degeneracy, which allows for movement in the design space against the steepest descent, the simplex may not search the entire design space. Schmucker and White (2007) modified the Nelder-Mead method with simulated annealing, adding random variations into components to reduce the chances of becoming stuck in a local minima like the pure downhill simplex does. While adding randomness is effective, the result of the optimization may not the same every time the optimization algorithm is run. To prevent the downhill simplex scheme from getting stuck while minimizing the randomness in the solution, the optimization procedure is run several different times with varying initial conditions and selecting the single best solution from the multiple converged solutions. The initial conditions chosen correspond to the 'standard' drop shapes found for various experiments. The optimization method does not require the initial guess to be close to the true solution. But, starting the simplex method with a vertex near to the drop shape accelerates convergence.

After generating an initial set of vertices, the optimizer evaluates their objective function, the error function $\chi^2 = \nu * N_{negative} + \sum_{j=1}^{J} \sum_{k=1}^{K} \mu_{j,k} |\overrightarrow{s}_{measured} - \overrightarrow{s}_{reconstructed}|$. The error function is minimized by decreasing the differences between the measured and reconstructed shift vectors. The measured shift vectors are taken from the DIC output and bi-linearly interpolated at each grid location.

The value of the error function depends on a penalty factor ν and a weighting function $\mu(j, k)$. Harsh penalties are applied via large values of ν for any reconstruction with non-physical solutions, such as negative heights. The values of the weighting function $\mu(j, k)$ at each grid location are to prioritize certain grid nodes while decreasing the importance of others. One of the criteria used for weights are the correlation coefficient of the DIC reconstruction, increasing $\mu(j, k)$ for nodes with strong correlations and decreasing $\mu(j, k)$ for nodes with potentially spurious ones.

To find $\overrightarrow{s}_{reconstructed}$, the shift vectors created from the guessed basis functions, both the non-linear and simplified equations are used. The Nelder-Mead optimization method requires many evaluations of the objective function. As mentioned previously, solving for the components of $\overrightarrow{u}_p$ requires solving of a non-linear system of equations numerically for each grid node in both drop images which can be very time consuming. To speed up the process, the Nelder-Mead optimizer is run to convergence using the simplified Equation 3.5 for the reconstructed shift vectors. Then, the converged verticies of the simplex are re-input to another optimization loop using the non-linear solution for $\overrightarrow{s}_{reconstructed}$. This greatly speeds up the convergence of the optimization method as the differences between the estimated shift field and true shift field are generally very small.

3.5 Force measurements

The final step in the reconstruction process is to extract the drop pinning force from the solution profile. Recalling Equation 1.1, the integral for the total pinning force on a drop is a function of the surface tension, γ, the direction vector $\hat{n}$, and the contact angle at each location θ_i. The integral $\overrightarrow{F_i} = \gamma \oint \cos \theta_i \hat{n}_i \delta s$ is solved numerically, with each radial grid line having a direction and contact angle. The direction vectors result from the elliptic grid and are always perpendicular to the contact line. They are found numerically at each radial grid line from the inverse tangent of the grid coordinates. The contact angle for each radial grid line is calculated in the same way from the drop height. Finally the arc length δs is the distance between the circumferential grid coordinates.

4. RESULTS

4.1 Drop Reconstruction Example

After a reconstruction is completed, the resulting drop profile can be used to study drop evolution, pinning force, runback, and more. To show this, the results of a single drop reconstruction is shown. The drop in Figure 4.1 below is 150 μL and is tilted at 10°. This drop was chosen as an example as the advancing contact angle is approximately 60°, 10° larger than the limit of the single camera method by Schmucker and White (2007). The receding contact angle is approximately 41°, giving a relatively large contact angle hysteresis of 19° which precludes it from any current analytical solutions. The advancing camera was tilted to $\overrightarrow{\theta}_c = [-13°, -2°]$. and the receding camera the inverse at $\overrightarrow{\theta}_c = [13°, -2°]$.
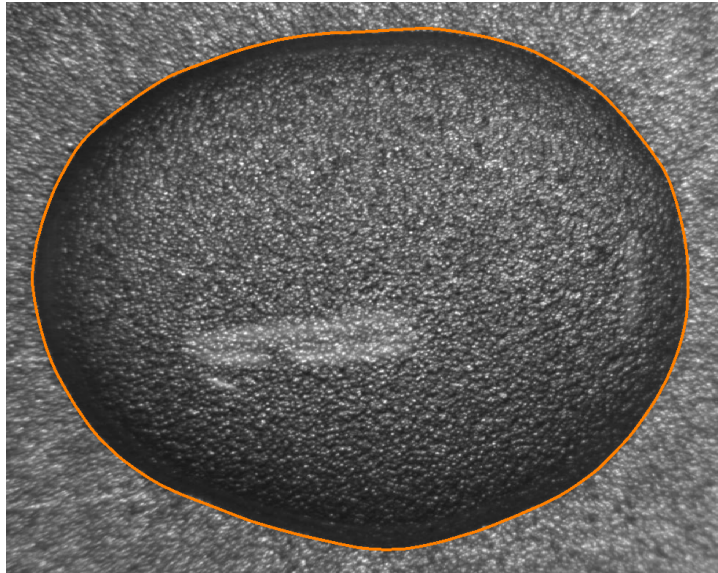

Figure 4.1: 150 μL drop tilted at 10° (advancing side camera image)

Figure 4.1 shows the advancing side image of the 150 μL drop. The DIC analysis is shown below for both the advancing and receding cameras. The specular reflection is present but slight and does not effect the results,
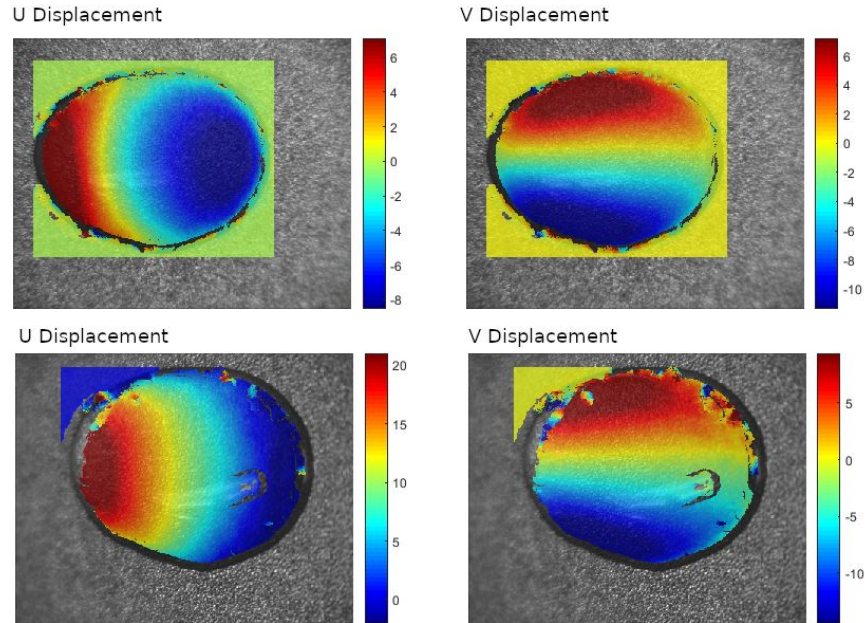

Figure 4.2: DIC shift vectors for the advancing (top) and receding (bottom) cameras.

With the shift vectors measured, the center of the grid is found from the sum of the advancing and receding shift fields as seen in Figure 4.3. The center is selected to be very near the apex of the drop, where the added shift vectors becomes zero. Note that as both cameras were tilted in the negative z direction, the shift vectors in the z direction do not cancel out at the drop height, accounting for the slight movement in the center z coordinate.
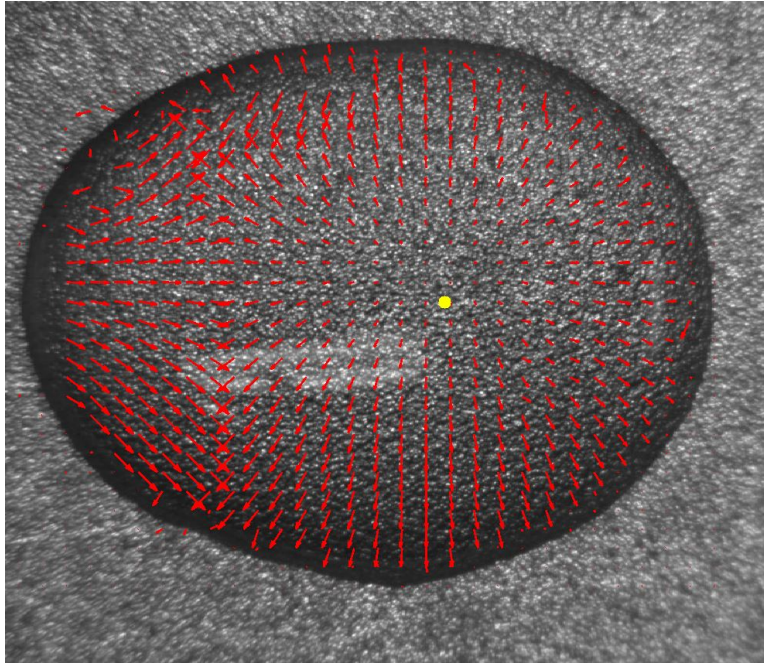
Figure 4.3: Grid center location with summation of advancing and receding shift vectors.

The elliptic grid is shown in Figure 4.4 projected onto the advancing drop image. The 80 radial grid lines curve to create right angles with the drop contact line while keeping equal spacing between the 15 circumferential lines.
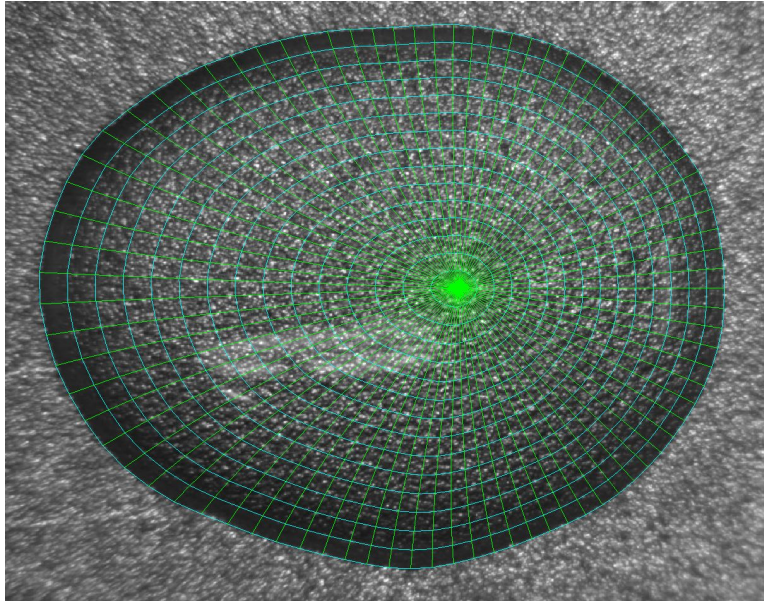
Figure 4.4: Elliptic grid projected onto drop image.

The initial optimization was done using the simplified calculation approach using 3 radial and 3 circumferential modes ($M = N = 3$). The simplex optimization scheme converged in 155 iterations taking approximately 5 minutes. Then, the output amplitude coefficients were used as the inputs to the second simplex optimizer using the full non-linear equations for the shift vectors. The second run verified convergence in 4 iterations which required approximately 5 minutes. Figure 4.5 below shows the pixel difference between the shift vectors calculated by the linear simplification and the non-linear solution for the final converged drop profile. As shown, there is very little difference between the linear assumption and true solution as the shift vectors range from 0 to 35 pixels, sometimes even more. However small, the sub-pixel differences between the two solutions can appreciably impact the overall reconstruction and so implementing the non-linear solution is crucial for correct reconstructions. Especially as an increase in drop slope increases the error between the solutions, which happens at the edges of the drop where the

reconstruction is most critical.
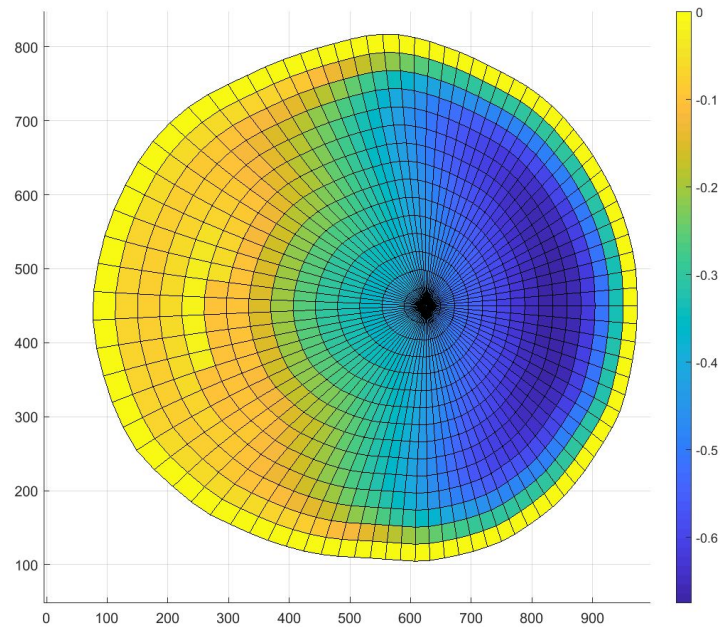
Figure 4.5: Difference between linear and non-linear shift vector calculations.

The full reconstruction is shown below in Figure 4.6, projected onto the drop image. The overall goal of the entire work is shown below with a 3D drop profile calculated from a 2D speckle image. To convert to physical dimensions the scale images are used, as shown in Figure 4.7.

Figure 4.6: 3D drop profile projected onto speckled drop image.

1724.6 pixels/in

Figure 4.7: Scale image example.

Table 4.1 below shows the optimized Bessel amplitudes for the optimized solution.

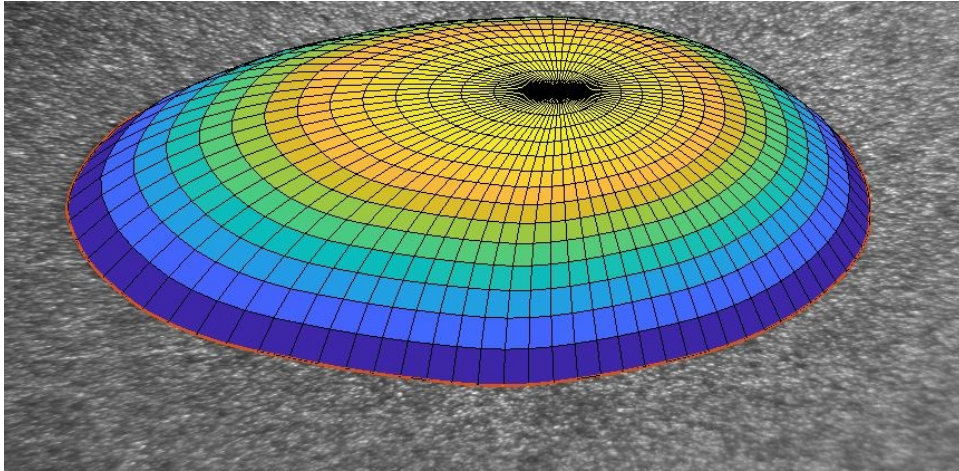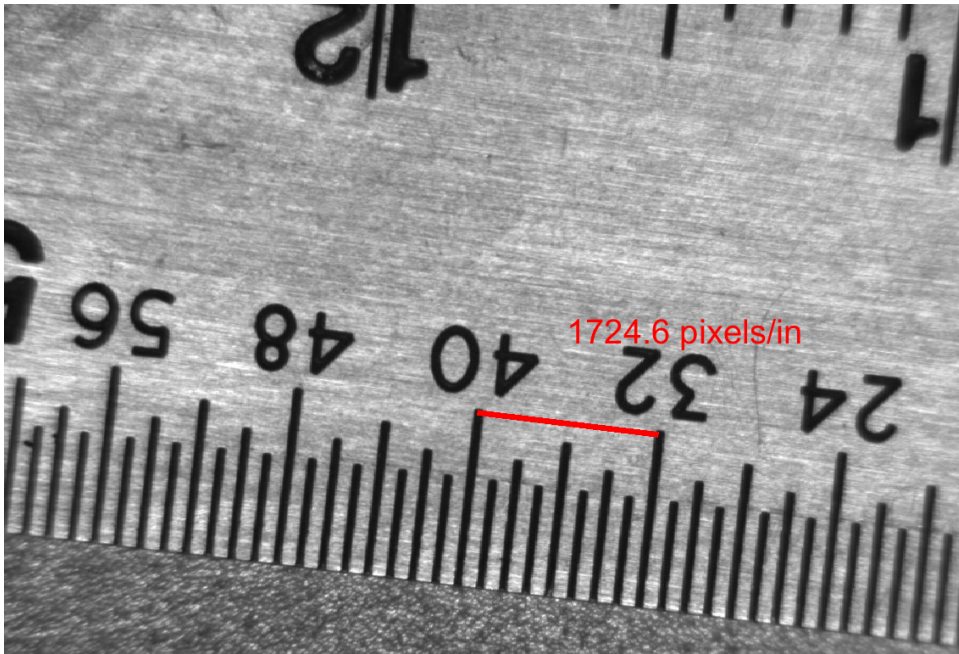|	N=1	N=2	N=3
M=0	-71.7103	0.2795	0.7382
M=1	0.2588 + 0.4803i	0.7416 - 0.6090i	0.4859 + 0.2534i
M=2	0.2648 + 0.7489i	0.2678 + 0.2729i	0.4733 + 0.3489i

Table 4.1: Optimized Amplitude Coefficients

The $A_{(0,1)}$ amplitude is shown to be significantly larger than any other amplitude coefficient. The large negative amplitude flattens out the spherical cap mode, decreasing the maximum height in the middle while increasing the contact angles at the edges. The optimized solutions often result in the $A_{(0,1)}$ amplitude coefficient being one to two orders of magnitude larger than the other coefficients. The spherical cap mode has a coefficient of 0.4124, which seems small. However, recalling the A_{SC} coefficient ranges from 0 to 1 this is not the case. The spherical cap mode is scaled by the average drop radius R_{max}. For this drop R_{max} = 448.3, resulting in the A_{SC} coefficient being the dominant value in the reconstruction, even more so than $A_{(0,1)}$.

After the reconstruction is completed, it is important to know how well the calculated 3D profile matches the physical drop. This is difficult because there is not a drop solution benchmark. Instead, to evaluate the accuracy of the measurement technique the reconstructed profile is compared to several known properties of the drop. Sideview profile images, drop volumes, and wind tunnel tilt angles are all quantities that are captured during an experiment but are not required for the reconstruction. These are used as comparison targets for assessing the reconstructed drop accuracy. Sideview profiles give a strong indication to the correctness of the solution. However, as mentioned previously, 2D measurements are not sufficient in determining the drop shape. Combining the sideview profile with the known values of the drop volume and applied gravitational forcing a more complete picture of the drop correctness.

These parameters were chosen for several reasons to assess the correctness of the reconstructions. Firstly, as they are separate measurements and not inputs to the reconstruction there is no risk towards biasing the results towards the known solutions. The three metrics together also provide a unique solution for a drop profile. While two drops with the same volume tilted at the same angle could look wildly different from one another, drops with the same height, contact angle hysteresis, volume, and under the same loading are going to be extremely similar if not the exact same. Finally, the drop volume and contact angle error can directly be compared to the results for the single camera reconstruction method from Schmucker et al. (2012).

Showing the projection of the 2D reconstructed profile onto the sideview image yields both qualitative and quantitative comparisons. To start, the reconstruction needs to be projected onto the sideview image. The furthest uphill and downhill points were found for the sideview drop images, as well as the drop apex. A 2D slice is taken out of the 3D reconstruction from the smallest x coordinate to the largest. This 2D profile is projected onto the sideview image, matching the marked uphill and downhill points to the smallest and largest x coordinates. This qualitatively compares the reconstructed drop shape to the sideview image while quantitatively compares the advancing and receding contact angles and drop height. This comparison is shown in Figure 4.8 and is clearly very good.

The sideview image also gives the advancing and receding contact angles of the drop. Correct contact angles are the key to predicting drop stability and as such the measured contact angles are the most important results. As there is no known correct solution to compare the contact angles to, the 2D hysteresis is used as a marker for solution accuracy. The calculated minimum and maximum contact angles are compared to the measured advancing and receding contact angles from the sideview image. This is shown for the 150 μL drop in Figure 4.8 below. The advancing contact angle error was -4.2° while the

receding contact angle error was 0.6°. Comparing to the single camera results, the recon-structed angles are well within the given error limits of 2° and -7° given in Schmucker et al. (2012). Notably, the contact angle is nearly 60° and this exceeds the measurement capability of the single camera method.
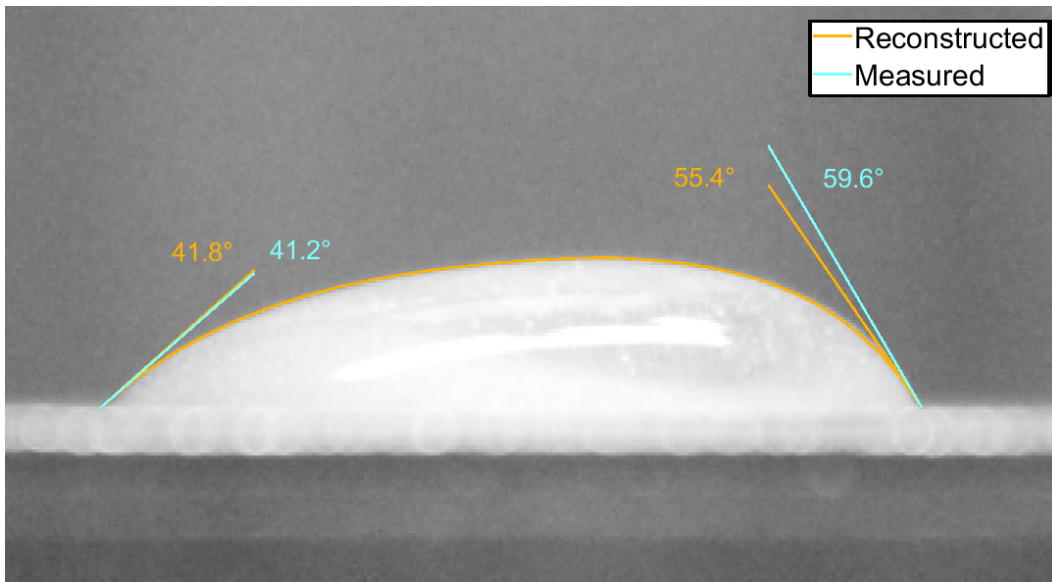

Figure 4.8: Sideview image of 150 μL drop with contact angles marked.

Another measure of correctness is comparing the predicted height of the reconstruc-tion to the measured height from the sideview. The highest point on the reconstructed profile, often the grid center but not always, is compared to the tallest point on the side-view image. The scale used in the sideview projection is used to compare the differences between them. For the 150 μL the reconstructed height was 2.316 mm compared to the measured height of 2.397 mm from the sideview camera. This gives a measurement error of 0.08 mm or 3.5%.

Moving away from the 2D sideview image, the drop volume is a strong indication of

the correctness of the 3D solution. The volume is measured to the nearest μL with the syringe used to apply the drop and is one of the only known properties of the drop. The volume of the reconstruction is found by integrating the basis functions and the spherical cap mode at each grid location. For the 150 μL drop above the calculated drop volume was 148.2 μL, or a -1.2 % error. The very small error supports the correctness of the reconstruction while showing significant improvement over the single camera method. Schmucker et al. (2012) found a consistent volume error of -10% to -30% for all drops. The stereoscopic camera method provides significantly more accurate volume reconstructions.

The final, and most important, output of the reconstruction is the predicted pinning force. The pinning force is key to drop stability experiments and, as such, the stereoscopic reconstruction method should be able to better estimate the force than 2D hysteresis calculations. The pinning force is calculated from the integral given in Equation 1.1 evaluated numerically at each grid location as described in Chapter 3. The resulting force measurements are given in Newtons using the calibration images to relate the pixel measurements to meters. To evaluate the accuracy of the force reconstruction, the calculated pinning force is compared to the applied gravitational forcing. As there is no other outside forcing terms the pinning force equals the gravitational force. The applied gravity force is given by the expression $F_g = -\rho g V \sin(\theta)$ where ρ is the density of water, g is the gravitational acceleration, V is the applied drop volume, and θ is the tilt of the wind tunnel. The applied drop volume is known to $\pm$ 1 μL and the wind tunnel tilt angle is known to $\pm$ 0.05 ° while the other terms are constants of the system. For the 150 μL drop above the calculated pinning force was 2.43 $\times 10^{-4} N$ compared to the applied forcing of 2.55 $\times 10^{-4} N$, -4.60 % of the applied gravitational forcing. The discrepancy between the reconstructed pinning force and the applied pinning force is most likely due to the

advancing contact angle error. The contact angle distribution is given in Figure 4.9 below. Note that the starting position, 0 radians, is the furthest grid node towards the right hand side and is approximately the advancing contact angle.
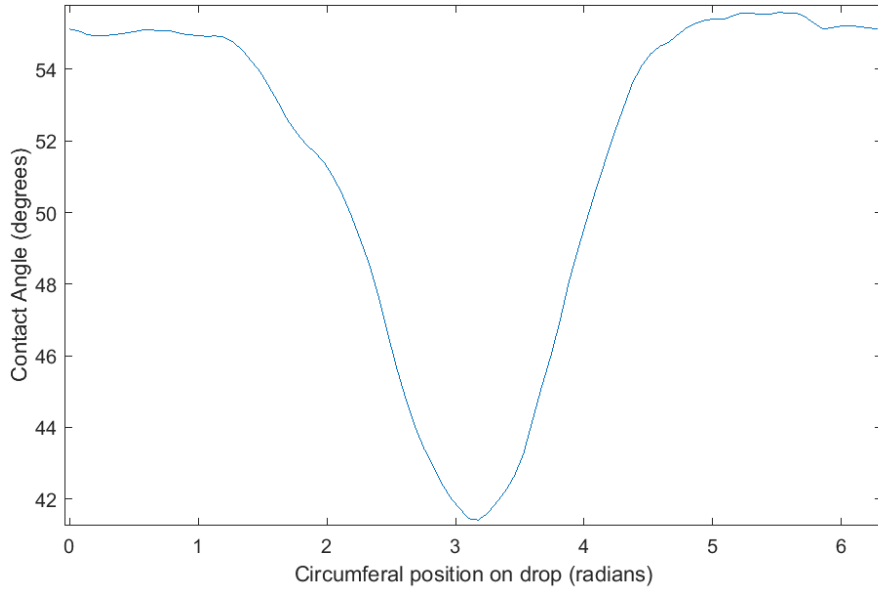

Figure 4.9: Reconstructed drop contact angle measured counter-clockwise around the contact line.

4.2   Error Analysis

To give a larger representation of how well the stereoscopic reconstruction captures the drop profiles, full 3D reconstructions were performed for 16 drops ranging from 50 μL to 200 μL at various tilt angles. The advancing and receding cameras were set to ($\pm 13°$, -2°) for all drops. The advancing contact angle, receding contact angle, apex height, volume, and pinning force were measured for each drop. These parameters were compared to the known values from the experiment to assess the accuracy of the stereoscopic method.

The sideview image of each drop was used to calculate the 2D contact angles and drop height.

The average errors and standard deviations of those errors can directly be compared to the work by Schmucker et al. (2012), which measures over 200 drops using the single camera method and compares the measured errors. This is an excellent source of comparison between the single and stereoscopic camera speckle shift reconstruction methods. As shown below, the stereoscopic camera method either decreases the average error or better centers the error about 0 % for all tested parameters. It is important to note that some of the drops tested by Schmucker et al. (2012) were under mixed wind-gravitational forcing while the drops tested in this work were only under gravitational forcing.

The first measured parameter, predicted drop height, has no published results from the single camera method to compare the error to. However the calculated height error is a strong indication of how well the center of the drop is reconstructed, in the same way that the contact angles are representative of the edges of the drop. The average percent error of the height measurements taken is 0.2% of the true drop height with a standard deviation of 5.5 %.

The more important measure from the sideview images are the advancing and receding contact angles. Figure 4.10 shows the difference between the measured and the calculated contact angles for the performed reconstructions. The measured angles from the sideview images ranged from 22° to 73°. The stereoscopic reconstruction was able to capture the contact angles with an average error of -0.65° and a standard deviation of 2.6°, maintaining 90% of the reconstructed angles within $\pm$ 5°.
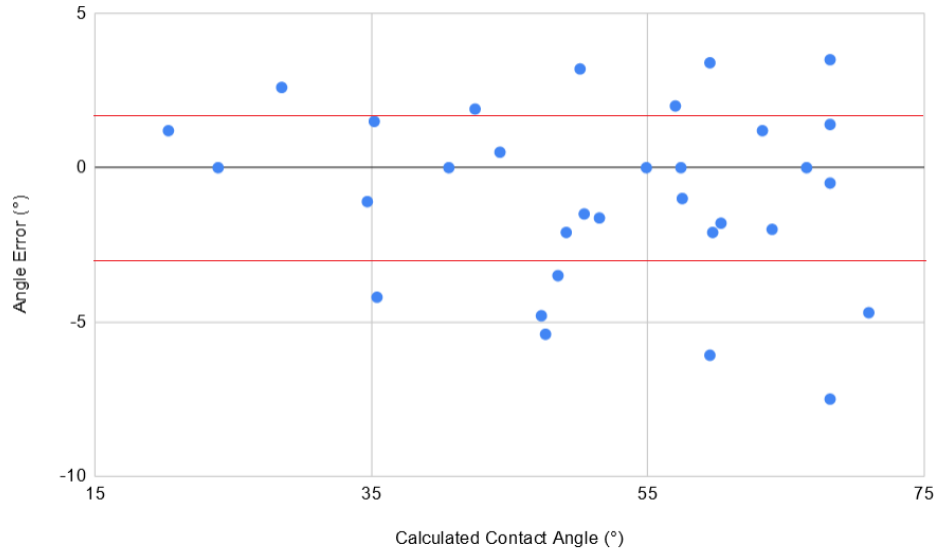
Figure 4.10: Contact Angle Error (°) vs Contact Angle (°)

It can also be useful to look at the difference between the advancing vs receding contact angle error. There is no difference in procedure between for calculating the two angles, however the advancing contact angles are larger, leading to larger error. This idea is furthered by the reconstructed angle error trending towards larger, negative errors as the contact angle increases. The average error of advancing contact angles is -1.9° with a standard deviation of 3.2° as compared to the average error of only 0.2° and standard deviation of 2.0° for receding contact angles. The same negative trend is found even when comparing the percent error of the advancing contact angles, accounting for the larger angle magnitudes. This is consistent with the findings of Schmucker et al. (2012), though with lesser magnitudes.

Comparing these results to those of the single camera method, Schmucker et al. (2012) found 68% of their measured contact angles to be within the limits of -6.9° and 2.0° with a maximum error of -20°. Error increased substantially as the contact angles increased over

50°. The present work found 68% of measured contact angles to be within -3.4° and 2.0° for contact angles up to 70° using the stereoscopic reconstruction method. The largest contact angle error measurement was -7.5° from a measured contact angle of 74°. This was above 70°, the target upper bound of the reconstruction method. The stereoscopic method also reduced the negative angle bias significantly, from the average measurement error of -3° for the single camera method to -0.7° for the stereoscopic method. This is largely due to removing large negative errors at higher contact angles and allows for more accurate predictions to be made from the measurement data.

It is important to note that this work used only gravitational forcing and a significantly smaller number of the drop samples for measurements than Schmucker et al. (2012). However, the high maximum angle error from the single camera method at higher advancing angles was not an outlier; many measurement errors were above 10° or even 15°. This demonstrates the stereoscopic method is at least more accurate at measuring all contact angles than the single camera method developed by Schmucker and White (2007) and significantly more accurate when capturing contact angles of greater than 50°.

The other measure of accuracy that can be directly compared to the single camera method is the reconstructed drop volume. The volume is calculated from the numerical integration of the basis functions and spherical cap mode. The average volume error was -0.9% with a standard deviation of 8.5%. The single camera method found almost all of their reconstructions to be within -10% and -30% of the applied drop volume Schmucker et al. (2012). The stereoscopic method has a similar wide variance in volume measurement error but the error is centered about zero instead of a strong negative bias. This, along with over half of the measured drops having volume errors between ±6%, shows that the stereoscopic method predicts the drop volume better than the single camera method by Schmucker et al. (2012). The higher variance is due to the optimization

method not solving for the volume directly. The drop reconstruction can be improved with an additional input to the optimization method of a known drop volume, however the reconstruction method is designed to not require volume measurements. There is no correlation between volume error and angle error, however height error and volume error are often tied together. This is not always the case however as sometimes the drop shape deforms to fit the drop height and contact angles increasing the volume error dramatically. Figure 4.11 shows the volume error vs volume applied.
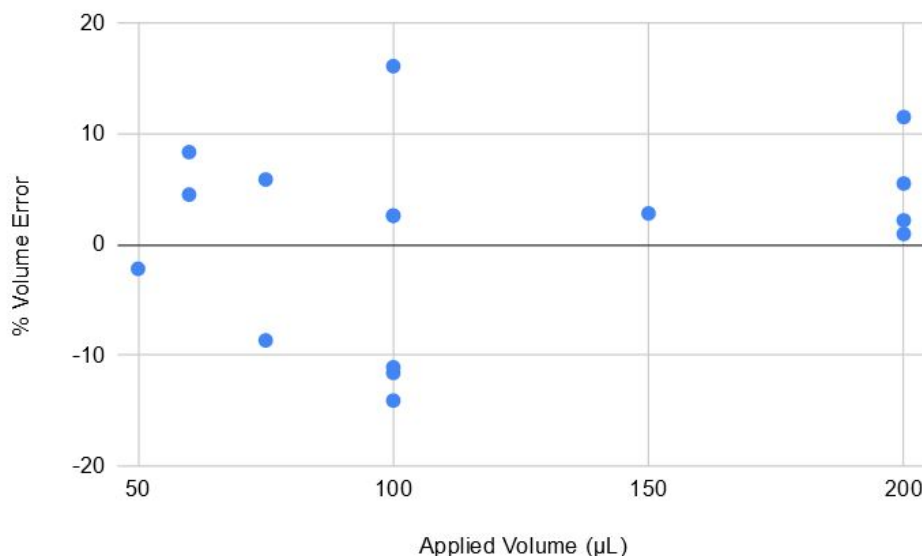

Figure 4.11: Volume $\%$ Error vs Applied Volume

The pinning force is known exactly from the applied drop volume and tunnel tilt angle. The forcing measurements made from the stereoscopic camera reconstruction are capable of predicting drop pinning forces with an average error of 14.3%. However it may be more useful to use the drop reconstruction to predict the applied tilt angle θ. The calculated tilt angle vs applied tilt angle is shown below in Figure 4.12. The stereoscopic reconstruction

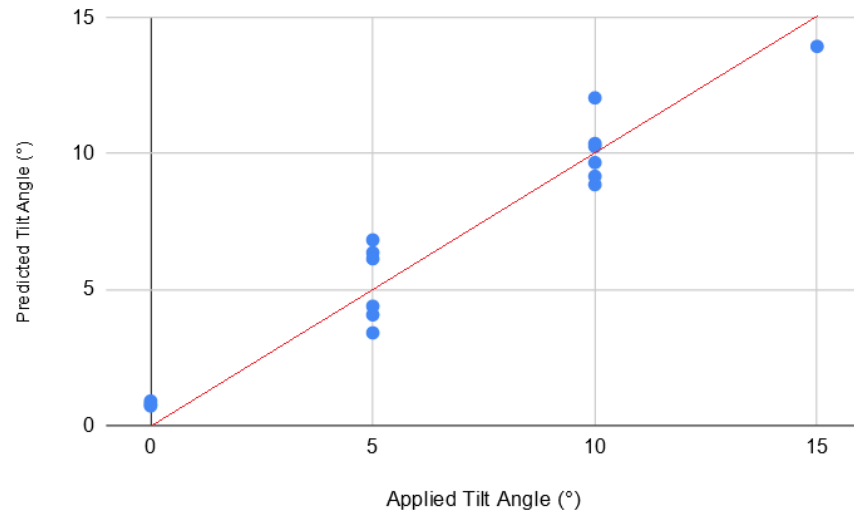method found the average predicted angle error to be -0.17° with a standard deviation of 1.13°.

Figure 4.12: Calculated Tilt Angle vs Applied Tilt Angle

5.   SUMMARY AND CONCLUSIONS

This thesis presents a modified procedure for reconstructing drop profiles and evaluates the accuracy of that method. Drop depinning is of interest for a wide range of applications, from heat exchangers and fuel cells to ice accretion on aircraft. The understanding of when drops remain stationary or run back along the surface is critical in predicting the overall behavior of a larger system such as an airfoil in icing conditions. The pinning force is a function of the drop contact line shape and contact angles the drop makes with the surface so the measurement technique presented here is needed to better understand these phenomena.

The research presented here is a modification of the single camera speckle shift reconstruction method developed by Schmucker and White (2007). While the original measurement technique used a single camera directly parallel to the test surface, this work expanded that and used two cameras pointed at oblique angles. This approach mitigates the total internal reflection Schmucker and White found around the edges of drops with large contact angles. The critical viewing angle for a water-air interface is 55° and the refracted luminance decreases as that limit is approached. This limitation led to significant errors in the reconstructed contact angles for drops with measured contact angles of above 50°.

The technique presented in this research takes two sets of images, one for each camera. These images capture the speckled pattern created by the rough surface with a drop present and without, allowing a Digital Image Correlation code to measure the shift vectors of each pixel in the drop image. The drop shape is represented as a sum of a spherical cap and Bessel–Fourier series modes calculated over nodes of an elliptic grid constructed within the detected contact line. A simplex optimization method is applied to find the drop

68

shape by minimizing the difference between the shift vector field of the reconstructed drop shape and the measured vector field.

The stereoscopic reconstruction method captures the contact angles and drop volume more accurately than the single camera method by Schmucker and White (2007). The stereoscopic camera approach also allows a wider range of drops to be measured, increasing the maximum allowable contact angle from 50° to 70°. The single camera method found 68% of their measured contact angles to be within the limits of -6.9° and 2.0° with a maximum error of over 20°. This error increased as the contact angles measured increased over 50°. This work using stereoscopic cameras found 68% of their measured contact angles to be within the limits of -3.4° and 2.0° for contact angles up to 70°. The largest contact angle error measurement was -6.7° from a measured angle of 73°. The stereoscopic method also reduced the negative angle bias significantly. Previously, the average measurement error was -3° for the single camera method as compared to -0.7° for the stereoscopic method. The stereoscopic method also captures the maximum drop height to within ±5.5% for 68% of drops and predicts the pinning force with an average error of 14.3%.

The main challenges in adapting the single camera method to a stereoscopic reconstruction method were optimizing using two data sets and the complex ray tracing required to accurately represent the drop shapes. The simplex optimization method and most other optimization algorithms are designed for a single non-linear objective function. The stereoscopic reconstruction uses a combination of two related but separate non-linear objective functions which can be difficult to converge on a correct solution. This can be mitigated with multiple restarts and weighting functions, however this greatly increases the computational cost. The objective function requires a system of non-linear equations to be solved for every grid point for two full drop areas. The solution to this problem used

in this work is to estimate of the objective function with a simplified equation that is computationally cheap. This provides a very close solution which is then optimized to convergence with the computationally expensive full objective function. Starting with a very close approximation significantly accelerates convergence and cuts down on computation time. This solution produces an good reconstruction with a relatively short computational time, however is not guaranteed to be the most optimal solution.

Future studies continuing the stereoscopic reconstruction method could expand this work for mixed gravity and wind forcing. This could be further expanded into studies of drop drop depinning following the work by Schmucker (2012). Furthermore, the results generated are most likely specific to this particular setup. Future studies on drop stability thresholds should be based on experiments which match the expected conditions, such as ice build up. Further work is required to make broad statements about drop stability and the ability to measure full 3D profiles on all rough surfaces. The research presented in this thesis is an adaptation and modification of speckle shift reconstruction method for calculating full 3D drop profiles. This work expands the workable contact angle limits while decreasing average error when compared to the single camera method by Schmucker and White (2007) across a number of comparable parameters.

REFERENCES

Viatcheslav Berejnov and Robert E Thorne. Effect of transient pinning on stability of drops sitting on an inclined plane. *Physical Review E*, 75(6):066308, 2007.

JJ Bikerman. Sliding of drops from surfaces of different roughnesses. *Journal of Colloid Science*, 5(4):349–359, 1950.

Justin Blaber, Benjamin S. Adair, and Antonia Antoniou. A methodology for high resolution digital image correlation in high temperature experiments. *Review of Scientific Instruments*, 86(3):035111, 2015. doi: 10.1063/1.4915345.

Tung-He Chou, Siang-Jie Hong, Yu-Jane Sheng, and Heng-Kwong Tsao. Drops sitting on a tilted plate: Receding and advancing pinning. *Langmuir*, 28(11):5158–5166, 2012.

E. B. Dussan V. On the ability of drops or bubbles to stick to non-horizontal surfaces of solids. Part 2. Small drops or bubbles having contact angles of arbitrary size. *Journal of Fluid Mechanics*, 151:1–20, 1985.

E.B. Dussan V. and R. T.-P. Chow. On the ability of drops or bubbles to stick to non-horizontal surfaces of solids. *Journal of Fluid Mechanics*, 137:1–29, 1983.

AI ElSherbini and AM Jacobi. Retention forces and contact angles for critical liquid drops on non-horizontal surfaces. *Journal of Colloid and Interface Science*, 299(2): 841–849, 2006.

Burak Eral, D. Mannetje, and Jung Min Oh. Contact angle hysteresis: A review of fundamentals and applications. *Colloid and Polymer Science*, 291, 02 2013. doi: 10.1007/s00396-012-2796-6.

Charles W. Extrand and Y. Kumagai. Liquid drops on an inclined plane: The relation between contact angles, drop shape, and retentive force. *Journal of Colloid and Interface Science*, 170(2):515–521, 1995. doi: 10.1006/jcis.1995.1130.

Kshitiz Garg and Shree K. Nayar. Photorealistic rendering of rain streaks. *ACM Transactions on Graphics*, 25(3):996–1002, 2006. doi: 10.1145/1141911.1141985.

Andrea G. Kraj and Eric L. Bibeau. Phases of icing on wind turbine blades characterized by ice accumulation. *Renewable Energy*, 35(5):966–972, 2010. doi: 10.1016/j.renene. 2009.09.013.

G Macdougall and C Ockrent. Surface energy relations in liquid/solid systems I. The adhesion of liquids to solids and a new method of determining the surface tension of liquids. *Proceedings of the Royal Society of London. Series A. Mathematical and Physical Sciences*, 180(981):151–173, 1942.

AJB Milne and A Amirfazli. Drop shedding by shear flow for hydrophilic to superhydrophobic surfaces. *Langmuir*, 25(24):14155–14164, 2009.

J. A. Nelder and R. Mead. A Simplex Method for Function Minimization. *The Computer Journal*, 7(4):308–313, 01 1965. ISSN 0010-4620. doi: 10.1093/comjnl/7.4.308. URL `https://doi.org/10.1093/comjnl/7.4.308`.

E. Pierce, F.j. Carmona, and A. Amirfazli. Understanding of sliding and contact angle results in tilted plate experiments. *Colloids and Surfaces A: Physicochemical and Engineering Aspects*, 323(1-3):73–82, 2008. doi: 10.1016/j.colsurfa.2007.09.032.

T. Podgorski, J.-M. Flesselles, and L. Limat. Corners, cusps, and pearls in running drops. *Physical Review Letters*, 87(3), 2001. doi: 10.1103/physrevlett.87.036102.

David Quéré, Marie-José Azzopardi, and Laurent Delattre. Drops at rest on a tilted plane. *Langmuir*, 14(8):2213–2216, 1998.

E. Rio, A. Daerr, B. Andreotti, and L. Limat. Boundary conditions in the vicinity of a dynamic contact line: Experimental investigation of viscous drops sliding down an inclined plane. *Physical Review Letters*, 94(2), 2005. doi: 10.1103/physrevlett.94. 024503.

Jason A. Schmucker and Edward B. White. Technique for measurement of droplet profiles for use in icing physics studies. *SAE Technical Paper Series*, 2007. doi: 10.4271/ 2007-01-3293.

Jason A Schmucker, Joshua C Osterhout, and Edward B White. Speckle technique for dynamic drop profile measurement on rough surfaces. *Experiments in Fluids*, 52(1): 123–136, 2012.

Jason Allen Schmucker. *Experimental investigation of wind-forced drop stability*. PhD thesis, Texas A&M University, 2012.

Pavel A. Strizhak, Maxim V. Piskunov, Roman S. Volkov, and Jean C. Legros. Evaporation, boiling and explosive breakup of oil–water emulsion drops under intense radiant heating. *Chemical Engineering Research and Design*, 127:72–80, 2017. doi: 10.1016/j.cherd.2017.09.008.